



AMERICAN METEOROLOGICAL SOCIETY

Journal of the Atmospheric Sciences

EARLY ONLINE RELEASE

This is a preliminary PDF of the author-produced manuscript that has been peer-reviewed and accepted for publication. Since it is being posted so soon after acceptance, it has not yet been copyedited, formatted, or processed by AMS Publications. This preliminary version of the manuscript may be downloaded, distributed, and cited, but please be aware that there will be visual differences and possibly some content differences between this version and the final published version.

The DOI for this manuscript is doi: 10.1175/JAS-D-13-065.1

The final published version of this manuscript will replace the preliminary version at the above DOI once it is available.

If you would like to cite this EOR in a separate work, please use the following full citation:

Johnson, R., and P. Ciesielski, 2013: Structure and Properties of Madden-Julian Oscillations Deduced from DYNAMO Sounding Arrays. *J. Atmos. Sci.* doi:10.1175/JAS-D-13-065.1, in press.



Structure and Properties of Madden-Julian Oscillations Deduced from DYNAMO Sounding Arrays

3 RICHARD H. JOHNSON * AND PAUL E. CIESIELSKI

Colorado State University, Fort Collins, Colorado

*Corresponding author address: Richard H. Johnson, Department of Atmospheric Science, Colorado State University, Fort Collins CO 80523.
email: johnson@atmos.colostate.edu

ABSTRACT

5 The kinematic and thermodynamic characteristics of the October and November 2011
6 Madden-Julian Oscillations (MJOs) that occurred over the Indian Ocean during DYNAMO
7 (Dynamics of the MJO) are investigated. Analyses are presented (1) for two primary sound-
8 ing arrays, where results are independent of model parameterizations, and (2) on larger
9 scales, including the Indian Ocean, using operational and reanalysis data.

10 Mean precipitation during DYNAMO was characterized by maxima in two east-west
11 bands north and south of the equator. This pattern alternated between two bands during the
12 inactive phase of the MJOs and a single rainfall maximum on the equator during the active
13 phases. Precipitation over the northern sounding array (NSA), where the MJO signal was
14 strongest, was significantly modulated by the MJOs, while the southern array experienced
15 more frequent, briefer episodes of rainfall mostly related to ITCZ convection. Over the NSA
16 the MJOs were characterized by gradual moistening of the low-to-midtroposphere over \sim 2-
17 week periods. The October MJO featured multiple westward-moving, two-day disturbances
18 while the November MJO was principally comprised of two prominent Kelvin waves. Patterns
19 of moistening, divergence, and vertical motion suggest a stepwise progression of convection,
20 from shallow cumulus to congestus to deep convection. Tilted thermal anomalies in the
21 upper troposphere/lower stratosphere reveal gravity or Kelvin waves excited by the MJO
22 convective envelopes, which modulate the tropopause and contribute to pre-active-phase
23 upper-tropospheric moistening. While there are a number of similarities in the characteristics
24 of the two MJOs, there are sufficient differences to warrant caution in generalizing results
25 from these two events.

²⁶ 1. Introduction

²⁷ The Madden-Julian Oscillation (MJO; Madden and Julian 1972) is the most dominant
²⁸ signal of intraseasonal variability in the tropics. Its impacts are far-reaching. They extend
²⁹ into the subtropics and midlatitudes; specifically, there are influences on tropical cyclone fre-
³⁰ quency, monsoon onset and rainfall variability, ENSO, midlatitude storm tracks, the North
³¹ Atlantic Oscillation, the Arctic and Antarctic Oscillations, the Indian Ocean Dipole, Wyrtki
³² Jets, Indonesian Throughflow, and seasonal heat transport in the Indian Ocean (Webster
³³ et al. 1999; Lau and Waliser 2005; Wang 2005; Zhang 2005; Waliser 2006). Despite con-
³⁴ siderable attention given to the MJO over the past several decades, deficiencies remain in
³⁵ its basic understanding and prediction. Coupled general circulation models have a difficult
³⁶ time accurately simulating the MJO (Lin et al. 2006; Hung et al. 2013) and there is limited
³⁷ skill in prediction models (Kim et al. 2009). Moreover, recent work questions the nature
³⁸ of the MJO itself, suggesting that MJO disturbances are not dynamically distinct modes
³⁹ from equatorial Kelvin waves (Roundy 2012a,b). Hence, the basic dynamics of the MJO still
⁴⁰ remains an enigma.

⁴¹ Significant progress was achieved in observing basic features of the MJO in the western
⁴² Pacific based on data from the 1992-93 TOGA COARE (Tropical Ocean Global Atmosphere
⁴³ Coupled Atmosphere-Ocean Response Experiment), particularly the ocean-atmosphere cou-
⁴⁴ pling, the evolving precipitation systems, westerly wind bursts, surface fluxes, and the behav-
⁴⁵ ior of equatorial waves (Godfrey et al. 1998). However, conditions over the western Pacific
⁴⁶ are different from those over the Indian Ocean where deep convection associated with the
⁴⁷ MJO most frequently originates. The Indian Ocean is surrounded by landmasses on three
⁴⁸ sides and features seasonally reversing mean flow associated with the strongest monsoon in
⁴⁹ the world. The thermocline in the western Pacific is relatively deep, such that entrainment
⁵⁰ cooling only occasionally contributes to the upper-ocean heat budget (Lukas and Lindstrom
⁵¹ 1991; Cronin and McPhaden 1997), whereas the Indian Ocean features the relatively shal-
⁵² low Seychelles-Chagos thermocline ridge that exhibits large intraseasonal SST variability

53 (Hermes and Reason 2008; Vialard et al. 2009). Furthermore, unlike the Indian Ocean, the
54 western Pacific can exhibit a unique coupling between the MJO and the ocean by exciting
55 oceanic Kelvin waves which then interact with convection (Roundy and Gribble-Verhagen
56 2010).

57 Given the pronounced intraseasonal variability of the SST in the Indian Ocean, there is
58 strong evidence that ocean-atmosphere coupling plays an important role in MJO dynamics
59 in that basin (Flatau et al. 1997; Stephens et al. 2004; Zhang 2005). A sequence of events
60 in MJO development has been hypothesized to proceed as follows. During the initiation
61 phase, shallow cumulus progressively deepen into congestus clouds, the lower troposphere
62 moistens, and the upper ocean warms. These processes result in a build-up of convective
63 instability. This period has come to be referred to as the “recharge phase of the MJO (Bladé
64 and Hartmann 1993; Hu and Randall 1994; Kemball-Cook and Weare 2001), during which
65 moistening of the lower troposphere is achieved via detrainment from cumulus and conges-
66 tus clouds (Johnson et al. 1999; Kikuchi and Takayabu 2004) and/or moisture advection
67 (Benedict and Randall 2009; Maloney 2009). During the active phase of the MJO, deep
68 convection ensues, the upper troposphere moistens, and the upper ocean cools as a result in-
69 creased convective activity leading to reduced shortwave radiation, enhanced surface fluxes,
70 and upper-ocean mixing (Shinoda and Hendon 1998). Following the most intense rainfall,
71 the precipitation systems become more stratiform in character, strong low-level winds de-
72 velop, the upper ocean cools further, and the mid-to-lower troposphere rapidly dries out (Lin
73 and Johnson 1996; Maloney and Hartmann 1998; Johnson et al. 1999; Benedict and Randall
74 2009).

75 The evolution of precipitation systems and diabatic heating throughout this process can
76 be broadly characterized as a transition from shallow cumulus to cumulus congestus to deep
77 convection to stratiform (Johnson et al. 1999; Kikuchi and Takayabu 2004; Kiladis et al.
78 2005; Benedict and Randall 2007; Haertel et al. 2008). Recent measurements from *CloudSat*
79 and CALIPSO have provided additional documentation of the cloud fields associated with

80 the MJO (Virts and Wallace 2010; Riley et al. 2011; Del Genio et al. 2012). These studies
81 suggest that rather than cloud populations smoothly evolving from one type to another
82 throughout the MJO life cycle, all cloud types occur to some extent in all MJO phases but
83 their frequency of occurrence varies with time so as to give the broad appearance of a smooth
84 transition. These findings support the “building block” concept of the MJO proposed by
85 Mapes et al. (2006). But more specifically, there is evidence from the studies of Kikuchi and
86 Takayabu (2004), Yoneyama et al. (2008), Virts and Wallace (2010), and Del Genio et al.
87 (2012) to indicate that this progression of the cloud population actually occurs in a stepwise
88 fashion, with distinct periods of \sim week or more when there is a dominance of each (cumulus,
89 congestus, cumulonimbus) cloud type.

90 Despite these advances, the mechanisms by which the atmosphere is moistened during
91 the initiation phase of the MJO are still not fully understood. In fact, this subject remains
92 a matter of considerable debate (Waite and Khouider 2010; Hohenegger and Stevens 2013).
93 To address this problem, a field campaign was recently conducted in the Indian Ocean dur-
94 ing the period October 2011-March 2012. Its overarching goal is to investigate mechanisms
95 contributing to the initiation of the MJO. The experiment was comprised of three principal
96 participating entities: DYNAMO (Dynamics of the MJO); CINDY2011 (Cooperative Indian
97 Ocean experiment on intraseasonal variability in the Year 2011); and AMIE (ARM MJO In-
98 vestigation Experiment) (Yoneyama et al. 2013; Zhang et al. 2013). Hereafter, the collective
99 field campaign effort will be referred to as DYNAMO. DYNAMO’s three main objectives
100 are (1) determination of the mechanisms by which the troposphere is moistened in the ini-
101 tiation stage of the MJO, (2) the role of cloud populations in MJO initiation, and (3) the
102 role of air-sea interaction in the development and evolution of the MJO. While studies have
103 been conducted concerning these processes, they have principally been based upon reanaly-
104 sis products and satellite data. The only prior field efforts in the Indian Ocean directed at
105 these objectives have been the 2006 MISMO (Mirai Indian Ocean cruise for the Study of the
106 Madden Julian oscillation (MJO)-convection Onset; Yoneyama et al. 2008) experiment and

107 the French VASCO-CIRENE experiment (Vialard et al. 2009), but these field campaigns
108 have been limited in scope compared to DYNAMO.

109 This paper reports on preliminary findings from DYNAMO related to the broad-scale
110 structure and properties of the two prominent MJOs that occurred during the October-
111 November 2011 period of DYNAMO (the Special Observing Period or SOP) as revealed
112 by the atmospheric sounding arrays. A unique aspect of DYNAMO that contrasts it with
113 TOGA COARE is its location in the Indian Ocean where coupling of the MJO with deep
114 convection first occurs (Madden and Julian 1972). While our eventual goal is to unravel
115 the mechanisms operative during the moistening phase of the MJOs, the achievement of
116 this objective will involve a comprehensive analysis of large-scale moisture budgets, cloud
117 populations, air-sea interaction, etc. Such an effort will require the integration of multiple
118 data sets including ground-based radars, lidars, soundings, aircraft, and satellites, a task
119 underway but not yet completed. Therefore, the objective of this paper is to document the
120 basic thermodynamic and kinematic structure of the large-scale environment to provide a
121 context for that future work. The unique measurements collected during DYNAMO provide
122 an unprecedented data set over the Indian Ocean with which to establish this large-scale
123 environmental setting.

124 2. Data and analysis procedures

125 a. Sounding observations

126 The DYNAMO sounding network was comprised of two quadrilateral arrays, one north
127 and one south of the equator (Fig. 1). The designs of the arrays were largely dictated by
128 the locations of suitable facilities on islands and atolls. Prior to the experiment a study was
129 conducted to evaluate the accuracy of quadrilateral arrays from the standpoint of budget
130 computations. It was demonstrated that such arrays represented an improvement over the
131 triangular array used during MISMO in capturing wave components of the MJO (Katsumata

¹³² et al. 2011).

¹³³ The six sounding sites comprising the two quadrilateral arrays shown in Fig. 1 are listed in
¹³⁴ Table 1. These arrays were intact for the majority of the 1 October-15 December time frame,
¹³⁵ so this period is selected as the focus of our study.¹ The southern quadrilateral reverted to
¹³⁶ a triangular array from 25 to 30 October during the R/V *Mirai* port call, after 30 November
¹³⁷ when the *Mirai* left its southern post, and from 31 October to 7 November during the R/V
¹³⁸ *Revelle* port call. Also, during this latter period, the northern array collapsed to a triangle.
¹³⁹ Finally, from 8 to 16 December, the *Revelle* was once again off station, so a southern array
¹⁴⁰ did not exist then. During these periods, computed fields of divergence and vertical motion
¹⁴¹ are less reliable (Katsumata et al. 2011), so the port call intervals will be highlighted in
¹⁴² subsequent figures. The four sites in the southern array launched eight soundings per day,
¹⁴³ while Malé and Colombo had a launch schedule of four per day, with Colombo falling back
¹⁴⁴ to once per day after 5 December. Five sites used *Vaisala* RS92 sounding systems (Table
¹⁴⁵ 1), while Colombo operated a *Meisei* RS06G system. All sites employed GPS wind-finding
¹⁴⁶ capabilities.

¹⁴⁷ As of this writing, sounding data quality control procedures, which mainly involve hu-
¹⁴⁸ midity corrections, are still underway. Preliminary intercomparisons with independent total
¹⁴⁹ column water measurements indicate that the RS92 systems exhibit a slight dry bias during
¹⁵⁰ the daytime. This dry bias is considerably less than that associated with earlier *Vaisala*
¹⁵¹ sonde types (Wang and Zhang 2008). In particular, first indications are that the dry bias
¹⁵² of the RS92 sensors (approximately 1-2% in the lower troposphere and 5-6% in the upper
¹⁵³ troposphere) is roughly only a third of that of the RS80 sensors used in TOGA COARE
¹⁵⁴ (Wang et al. 2002; Ciesielski et al. 2003). The *Meisei* system also has a dry bias (\sim 2 to 5%;
¹⁵⁵ Ciesielski et al. 2010) although corrections at Colombo have yet to be completed. Several
¹⁵⁶ *Vaisala* sites (Malé, Gan Island, *Mirai*) had built-in software to correct for a daytime dry

¹While this period is 15 days longer than the official DYNAMO SOP, to simplify terminology it will be referred to hereafter as the SOP.

157 bias, while a daytime bias correction adopted from Wang et al. (2013) was applied to the
158 sondes from Diego Garcia and the *Revelle*. These humidity-corrected data will be used in
159 this study. Future work that will focus on the moisture budgets for the MJO events will
160 utilize relative humidity corrected data at all sites.

161 In addition to corrections for sounding humidity biases, work is in progress to correct
162 for other sounding errors and siting impacts on the data and analyses thereof (e.g., ship
163 heating effects, influences of Sri Lanka island flow blocking on low-level Colombo winds);
164 however, these corrections or modifications to the soundings are largely excluded from this
165 paper. Nevertheless, these effects, while potentially important for detailed investigations of
166 the boundary layer properties and heat and moisture budgets, are not expected to alter the
167 general conclusions of this study.

168 Finally, dropsonde data from the National Oceanic and Atmospheric Administration
169 (NOAA) P-3 aircraft were incorporated into the gridded analyses described below. There
170 were 469 dropsonde observations from thirteen flights in proximity to the sounding arrays
171 during the period 9 November-13 December.

172 *b. Other data sources*

173 Precipitation rate estimates are based on the TRMM (Tropical Rainfall Measuring Mis-
174 sion) 3B42v7 product, which combines microwave rainfall estimates from TRMM and other
175 satellites with high temporal resolution infrared rain rate estimates to create a 3-hourly,
176 $0.25^\circ \times 0.25^\circ$ rainfall product (Huffman et al. 2007). Outgoing Longwave Radiation (OLR)
177 data on a $2.5^\circ \times 2.5^\circ$ grid are obtained from the NOAA Earth System Research Laboratory
178 (Liebmann and Smith 1996).

179 European Centre for Medium-range Weather Forecasts (ECMWF) operational forecast
180 data at 0.25° horizontal resolution, 18 vertical levels from the surface to 50 hPa, and six-
181 hourly intervals are used for the broad-scale analyses over the Indian Ocean, as well as north-
182 south vertical cross sections extending beyond the sounding arrays. A majority ($\sim 95\%$) of

183 the data from the sounding arrays were transmitted to operational centers in real time, so
184 the ECMWF analyses in the core sounding domain are heavily influenced by the sounding
185 data and are in good agreement with our gridded analyses over the quadrilateral areas.²
186 In addition, National Center for Environmental Prediction (NCEP)/National Center for
187 Atmospheric Research (NCAR) reanalyses (Kalnay et al. 1996) at 2.5° horizontal resolution,
188 15 vertical levels from the surface to 50 hPa, and six-hourly intervals are used for vertical
189 motion anomaly analyses.

190 Large-scale sea surface temperature (SST) observations were obtained from two sources.
191 SST anomaly fields extending to the central Pacific are from the NOAA Earth System Re-
192 search Laboratory (ESRL) website (<http://www.esrl.noaa.gov/psd/>) based on the Reynolds
193 et al. (2007) high-resolution (daily, 0.5° horizontal grid) blended analysis. SST fields over the
194 Indian Ocean are from the Woods Hole Oceanographic Institution (WHOI) Objectively Ana-
195 lyzed air-sea Fluxes (OAFlux; daily, 1° horizontal grid) website (<http://oaflux.whoi.edu/data.html>)
196 based on Yu and Weller (2007). Buoy data over the Indian ocean are from the Research
197 Moored Array for African-Asian-Australian Monsoon Analysis and Prediction (RAMA) pro-
198 vided by the National Oceanic and Atmospheric Administration (NOAA) Pacific Marine
199 Environmental Laboratory (PMEL) website (<http://www.pmel.noaa.gov/tao/rama/>). Fi-
200 nally, SST data from R/V *Revelle* were made available via <ftp://dynamo.dms.uconn.edu/>
201 through a collaborative effort between NOAA/Physical Sciences Division/ESRL, Oregon
202 State University, and the University of Connecticut.

203 c. Analysis procedures

204 Six-hourly (00, 06, 12, 18 UTC) sounding data for the northern and southern arrays, along
205 with P-3 aircraft dropsonde data, were objectively analyzed onto a 1° by 1° grid at 25-hPa

²Comparison of sounding-array mean profiles of zonal and meridional winds and relative humidity between the ECMWF and our model-independent, interpolated analyses indicates agreement to within 0.5 m s⁻¹ and 5%, respectively.

206 intervals from 1000 to 50 hPa over the entire domain shown in Fig. 1 using the multiquadric
207 interpolation procedure as described in Ciesielski et al. (1997). Operational GTS (Global
208 Telecommunication System)-resolution sounding data from sites shown in Fig. 1 outside the
209 arrays were used to help constrain the analyses. Corrections to the divergence were made
210 such that vertical motion balanced to zero at the tropopause level, which was determined at
211 each grid point and time step (Johnson and Ciesielski 2002). However, the divergence profiles
212 presented in the paper are based on the uncorrected values. At this stage, only sounding
213 and aircraft dropsonde data are used in the analyses: at a future time scatterometer winds,
214 profiler winds, and COSMIC (Constellation Observing System for Meteorology Ionosphere
215 and Climate) data will be included.

216 Thermodynamic and kinematic fields that are presented in the form of time series for the
217 northern and southern arrays are based on daily-averaged and spatially averaged values of
218 the interpolated fields over the respective arrays.³ Model data are excluded from these array-
219 averaged results; therefore, *we emphasize that the time series of fields such as divergence and*
220 *vertical motion over the arrays are independent of model parameterizations*. However, such
221 is not the case for the ECMWF/NCEP/NCAR-based analyses that are used to provide a
222 larger-scale context for the array results. Those model-based fields are presented for (1) the
223 entire Indian Ocean and (2) in north-south vertical cross sections that extend well beyond
224 the sounding arrays.

225 3. Broad-scale features of the flow and SST

226 The DYNAMO SOP occurred during La Niña conditions, as reflected by negative sea-
227 surface temperature (SST) anomalies over the central and eastern Pacific (Fig. 2). In con-

³The averaging areas for both arrays are kept fixed regardless of ship port calls, although it is recognized that the reliability of the results is diminished during those periods. In recognition of this fact, port-call intervals are denoted in time series plots by shading.

228 trast, the western Pacific and Indian Ocean were characterized by generally positive SST
229 anomalies. This SST anomaly pattern is consistent with the findings of Meyers et al. (2007)
230 who showed that during La Niña conditions, there is an extension of the western Pacific
231 warm pool into the Indian Ocean during a neutral Indian Ocean Dipole (IOD) state, which
232 existed during the DYNAMO SOP (<http://www.bom.gov.au/climate/enso/indices.shtml>).

233 SOP-mean TRMM 3B42 rainfall and ECMWF surface streamlines over the Indian Ocean
234 (IO) are shown in Fig. 3a. Two east-west bands of precipitation stretched across most of
235 the IO north and south of the equator, the southern one being most intense. In addition,
236 heavy rainfall occurred along the coast of Sumatra near 100°E. Both precipitation bands
237 were situated along troughs in the surface flow, exhibiting characteristics of Intertropical
238 Convergence Zones (ITCZs). The departure of the rainfall from the 14-year TRMM 3B42
239 mean is shown in Fig. 3b, along with the NCEP/NCAR reanalysis 500-hPa vertical motion
240 anomaly field for this same period. Rainfall was slightly above normal over much of the
241 equatorial IO, particularly west of 70°E, although it averaged near the 14-year mean over
242 the two DYNAMO sounding arrays. The centers of upward (downward) motion from the
243 NCEP/NCAR analysis correspond well to the positive (negative) precipitation anomalies
244 over the IO. The slightly above-normal precipitation over much of the IO is generally con-
245 sistent with the anomalously warm SST during the SOP (Fig. 2). The cool SST anomaly
246 near 6°S and 60°E is likely related to the substantial rainfall in that vicinity (Fig. 3a).

247 The SOP-mean SST and precipitation are shown in Fig. 4. While rainfall tended to
248 occur in areas where SST exceeded 28-29 C, the heaviest precipitation was located along
249 the strongest SST gradients. With air flowing from cold to warm water at the northern
250 and southern peripheries of the ITCZ bands (cf. Figs. 3a and 4), boundary-layer processes
251 likely played a role in the precipitation development. Specifically, boundary layer growth
252 via enhanced surface fluxes, moistening, and destabilization likely contributed to cloud de-
253 velopment and precipitation as air reached the warmer waters nearer the equator (Xie 2004;
254 Small et al. 2008).

255 While the mean SST was fairly uniform along the equator over much of the IO east of
256 60°E, there was pronounced SST variability during the SOP associated with the MJOs (Fig.
257 5). The passage of two MJO active phases, one in late October and another in late November,
258 is evidenced by maxima in rainfall, an increase in surface zonal wind speed, and drops in sea
259 level pressure of 4-5 hPa. The SST time series from the RAMA buoy at 1.5°S, 90°E shows
260 a general warming trend until late November, followed by cooling into early December.
261 This overall pattern was modulated by distinct intraseasonal variability associated with the
262 October and November MJOs, specifically warming over several-week periods followed by
263 sharp cooling during rainy, windy periods. This behavior closely resembles the intraseasonal
264 SST variability reported by Vialard et al. (2009) in the Seychelles-Chagos thermocline ridge
265 region of the IO. Brief periods of cooling were also observed during other rainy periods,
266 particularly during the first three weeks of October. The other conspicuous feature of the
267 SST time series is the large-amplitude diurnal cycle during the warming and light-wind/light-
268 precipitation periods in October, November, and early December. The damping of the SST
269 diurnal cycle during windy, rainy periods was also observed during TOGA COARE, where
270 it was attributed to wind-induced upper-ocean mixing, cloud shading, and precipitation
271 (Webster et al. 1996). This behavior of the SST in relation to the MJO is very similar to
272 that observed in TOGA COARE (Weller and Anderson 1996; Johnson et al. 1999).

273 **4. Multiscale variability of mean flow properties and** 274 **rainfall**

275 *a. Evolution of precipitation features over the Indian Ocean*

276 A time series of the phase and amplitude of the October and November MJOs is shown in
277 Fig. 6 in the form of the Wheeler and Hendon (2004) Real-time Multivariate MJO (RMM)
278 Index for the period 1 October to 15 December. Although propagating modes other than

279 the MJO can affect the RMM Index (Roundy et al. 2009), it is used here to describe the
280 broad-scale view of the MJO events during DYNAMO. The RMM index indicates that both
281 MJOs were at least of moderate amplitude over portions of the Indian Ocean and appear to
282 have completed global circuits, i.e., were “successive” events according to the terminology
283 of Matthews (2008).⁴ The period between the two MJO events was relatively short, \sim 30
284 days. This short period is perhaps related to the fact that La Niña conditions existed in the
285 Pacific, permitting a decoupling of the MJO from deep convection earlier than if neutral or
286 El Niño conditions existed (Tam and Lau 2005), hence contributing to a faster global circuit.

287 Both MJO events occurred during the period of the seasonal migration of convection
288 from the northern to southern hemisphere, as indicated by a time-latitude plot of OLR
289 anomalies over the central IO from 1 October 2011 to 31 March 2012 (Fig. 7). The largest
290 OLR anomalies during the October-November period occurred north of the equator; hence,
291 the northern sounding array captured the strongest convective signal of the MJOs. The
292 depiction in Fig. 7 is expanded in a time-latitude plot of TRMM 3B42 precipitation aver-
293 aged over the longitudes of the sounding arrays (Fig. 8). Over the northern array, which
294 extends approximately from the equator to 5° N (Fig. 1), very little precipitation occurred
295 outside the active periods of the October and November MJOs, whereas the southern ar-
296 ray (extending approximately from the equator to 7.5° S) experienced relatively frequent
297 episodes of precipitation. Figure 8 also reveals that the behavior of the precipitation during
298 the two MJOs was quite different, with the October event characterized by a series of two-
299 day near-equatorial maxima, much like the December 1992 MJO during TOGA COARE
300 (Takayabu et al. 1996; Haertel and Johnson 1998), while the November MJO was dominated
301 by two strong precipitation events. The latter two features were designated Kelvin waves
302 by the real-time filtering technique of Wheeler and Weickmann (2001) applied to OLR data

⁴Recent work by Straub (2013) indicates that many MJO events that do not appear to be successive in the global-scale RMM index, i.e., appear to develop in situ over the Indian Ocean and are labeled “primary” by Matthews (2008), do actually have predecessor, eastward-propagating signals of smaller zonal scale that precede the local amplification of the RMM index over the Indian Ocean.

303 (http://cawcr.gov.au/staff/mwheeler/maproom/OLR_modes/index.htm). In addition, the
304 prominent precipitation signals migrating poleward are indications of Rossby gyres associ-
305 ated with the November equatorial convection (Gill 1980), as also observed during TOGA
306 COARE (Chen et al. 1996). An infrared satellite image on 25 November (Fig. 9) shows
307 the northern circulation feature, which became Tropical Storm *05A* near the southern tip
308 of India on 26 November and subsequently moved into the Arabian Sea. While the two
309 precipitation signals have characteristics of Kelvin waves, their relatively slow speed ($\sim 8 \text{ m}$
310 s^{-1}) and the existence of associated trailing poleward-moving low-level cyclones may place
311 these events on the continuum between the MJO and Kelvin waves described by Roundy
312 (2012b).

313 A time-longitude plot of the TRMM 3B42 rainfall (Fig. 10) along with ECMWF 500-hPa
314 vertical motion depicts the two MJO convective envelopes, each consisting of both eastward
315 and westward disturbances, common features of MJOs (Nakazawa 1988). A diurnal cycle
316 of westward-moving precipitation features is observed over the longitudes of Borneo and
317 Sumatra (100-120°E), consistent with the findings of Mori et al. (2004) and Sakurai et al.
318 (2005). In October, the diurnal cycle transitioned to a quasi-two-day cycle farther west near
319 the longitudes of the DYNAMO sounding arrays. In November, a two-day cycle near the
320 DYNAMO array was less prominent, rather the behavior was dominated by two long-lived
321 precipitation events. To the west, precipitation associated with each MJO appeared to first
322 develop near the longitudes 50-60°E, where the SST began to exceed 28.5 C (Fig. 4). The
323 agreement between the ECMWF vertical motion field and precipitation is quite good, not
324 only over the longitudes of the DYNAMO arrays where sounding data from multiple sites
325 have been assimilated into the operational system, but elsewhere throughout the domain.

326 b. *Contrast of wind and thermodynamic properties over northern and southern sounding*
327 *arrays*

328 Time series of zonal wind, relative humidity (with respect to ice for $T < 0$), perturbation
329 temperature, and precipitation averaged over the northern sounding are shown in Fig. 11.
330 The rainfall time series clearly indicates the passage of the MJO active phases during the
331 latter half of October and November. A two-day periodicity of rainfall is evident for the
332 October MJO whereas the November event is dominated by a 4-5 day cycle of precipitation.
333 A gradual build-up in lower-tropospheric moisture over 1-2 week periods is observed for both
334 MJOs starting during the second weeks of October and November, followed by more rapid
335 moistening of the mid-to-upper troposphere just after the middle of each month. Rapid
336 drying in the lower troposphere occurred toward the end of the precipitation episodes along
337 with increased westerlies, as found during TOGA COARE (Lin and Johnson 1996). En-
338 hanced easterlies developed aloft during and immediately following the MJO active phases,
339 with the wind-speed maxima shifting downward with time. A similar downward tilt is seen
340 in the temperature anomaly pattern between 50 and 200 hPa, particularly for the November
341 MJO. The descent of the cold anomalies leads to a corresponding descent of the cold-point
342 tropopause, followed by a sudden upward jump at the end of the heavy-rain period (illus-
343 trated in a schematic depiction at the end of the paper). This tilted temperature anomaly
344 structure near the tropopause was first noted by Kiladis et al. (2001), who explained the fea-
345 ture as a gravity wave response to the MJO convective heat source envelope.⁵ More recently,
346 it has been found that this phenomenon is also manifested in CALIPSO cirrus data (Virts
347 and Wallace 2010; Virts et al. 2010). These authors found that the coldest, cloudiest anom-
348 alies aloft occurred 30° to the east of main MJO convective heat source and descend with
349 time, which is qualitatively consistent with the temperature anomalies near the tropopause
350 observed during DYNAMO. The correspondence between the cool and moist anomalies aloft
351 (\sim 100-200 hPa) preceding the heaviest rainfall can also be seen for the October and Novem-

⁵The same feature is also observed in convectively coupled Kelvin waves (Straub and Kiladis 2002).

352 ber MJOs. The overall upper-tropospheric temperature anomaly pattern, particularly for
353 the November MJO, characterized by a warm anomaly centered near 300 hPa and cold/warm
354 tilted anomalies at and above the tropopause closely resembles the reanalysis-based MJO
355 structure deduced by Kiladis et al. (2005, their Fig. 7). Weak cool anomalies are observed
356 near the surface in association with precipitation and associated convective downdrafts.

357 The time series of zonal wind, relative humidity, and precipitation averaged over the
358 southern array is shown in Fig. 12. While evidence of the two MJOs can be seen in all fields,
359 the strength of the moisture signal (relative humidity and precipitation) is somewhat weaker
360 than over the northern array. Particularly noteworthy is the lack of a distinct build-up of low-
361 level moisture prior to the periods of heaviest precipitation in late October and November.
362 In addition, frequent periods of mid-tropospheric moistening are observed throughout the
363 SOP, providing further evidence that the southern array straddled a relatively persistent
364 ITCZ trough (Fig. 3a) with somewhat less modulation by MJO passage (Fig. 7).

365 The time series shown in Figs. 11 and 12 are based on daily-averaged fields. Relative
366 humidity time series at four stations based on the full resolution of the sounding data (3-
367 hourly at Gan Island, R/V *Revelle*, and Diego Garcia; 6-hourly at Malé) are shown in Fig.
368 13. A striking feature is the distinct difference between the time series at Diego Garcia
369 at 7.3°S and those near the equator (Gan Island and *Revelle*) and to the north (Malé)
370 indicating a weaker signal of intraseasonal variability to the south. In addition, the higher
371 resolution data reveal moistening episodes at all sites on time scales ranging from diurnal to
372 4-5 days to intraseasonal. Particularly noteworthy are two-day oscillations in mid-October
373 and 4-5 day disturbances in mid-to-late November at the northern-array sites, consistent
374 with the precipitation time series (Fig. 11). Moreover, at Malé (4.2°N), Gan, and *Revelle*,
375 a stepwise progression of the moistening is evident. In particular, during the October MJO,
376 moist conditions were primarily confined below 800-850 hPa for the first 10-15 days of the
377 month, suggestive of trade-wind like cumulus conditions as observed episodically during
378 TOGA COARE (Johnson and Lin 1987). This period is followed by a ~week-long interval

379 of moistening to the midtroposphere (\sim 500 hPa), although the onset of this period is about
380 5 days later at Malé, and then by moistening through the entire troposphere. The period
381 of deep moistening is interrupted by drying episodes on a 2-day time scale. Figure 13 also
382 indicates a similar sequence of events in November, apart from the data gaps at *Revelle*,
383 as well as during a December MJO-like event not studied here. This stepwise pattern of
384 moistening in association with MJO passage was also noted by Kikuchi and Takayabu (2004)
385 over Indonesia during TOGA COARE and by Yoneyama et al. (2008) during MISMO. Also
386 present at Malé and Gan are descending dry anomalies near the tropopause, which are
387 associated with the descending warm anomalies over the NSA (Fig. 11).

388 A comparison of the vertical profiles of the mean flow and thermodynamic properties
389 over the two sounding arrays is shown in Fig. 14 covering the period 1 October-30 November
390 when the arrays were most complete. Low-level westerlies and upper-level easterlies, and
391 hence the mid-to-upper level shear, were stronger in the northern array. Low-level southerlies
392 and upper-level northerlies were present over both the northern and southern arrays (though
393 stronger to the south), likely an indication of the weakening, yet still present, Asian summer
394 monsoon circulation. Profiles of equivalent potential temperature were similar between the
395 two arrays, while the midtroposphere over the northern array was slightly more moist, as also
396 evident by comparing Figs. 11 and 12. The greatest variability in θ_e and relative humidity
397 was in the mid- to upper troposphere associated with the passage of the MJOs, consistent
398 with Yuan and Houze (2013), being somewhat greater over the northern array.

399 Changes in the zonal wind and relative humidity at Gan Island from the pre-active
400 to active phases of the October and November MJOs are shown in Fig. 15. The times
401 for the pre-active and active profiles were selected based on driest and moistest midlevel
402 conditions in the respective months, so the full amplitude of the midtropospheric moistening
403 is emphasized. The most notable relative humidity change is the substantial moistening
404 in the mid-to-upper troposphere, increasing from a minimum around 20% near 300 hPa to
405 nearly saturated conditions in the latter part of both months. Unlike the October MJO, the

406 November event did not show much change in the low-level moisture (below 600 hPa) from
407 the pre-active to active phase. In October (top panel, Fig. 15), the low-level zonal flow was
408 similar during both periods owing to the fairly strong westerlies early in the month (Fig.
409 11). Upper-level easterlies were also moderately strong in early October, so there was not a
410 marked change from the first to the last half of the month. However, in November there was
411 a prominent shift in the zonal winds from light easterly at low levels early in the month to
412 strong westerlies later (bottom panel, Fig. 15). In addition, there was a marked development
413 of easterlies aloft between 100 and 150 hPa with the passage of the active phase of the MJO.
414 The shear profile during the November active phase resembles that observed during the
415 convectively active phase of MISMO. Yamada et al. (2010) hypothesized that the easterly
416 shear during MISMO led to westward-moving cloud shields (advected by easterlies aloft)
417 that interacted with eastward-moving convective disturbances to produce a 2-4 day cycle
418 of convection within the larger-scale convective envelope of the eastward-moving MJO. The
419 extent to which this convective behavior occurred during DYNAMO is yet to be determined.

420 The changing north-south properties of the flow from the first to the second half of
421 October are shown in Fig. 16. To obtain a broader latitudinal perspective than just the
422 sounding arrays, these plots are based on the ECMWF operational analyses. The areas
423 north and south of the sounding arrays are essentially devoid of reliable sounding data
424 (stations in India contain numerous errors), so we utilize the ECMWF product for this
425 broader view. As noted earlier, the ECMWF analyses from 5°N to 10°S agree well with
426 those based on the sounding data alone. During the first half of the month (left panel,
427 Fig. 16), two rainfall bands were evident north and south of the equator, although the
428 northern one between 10° and 15°N was relatively weak. Strongest low-level convergence of
429 the meridional flow and divergence aloft was coincident with the rainfall maximum near 5°S.
430 A marked change occurred during the last half of October (right panel, Fig. 16). The rainfall
431 maximum shifted to the equator with considerable precipitation extending well north of the
432 equator. The mid- to upper troposphere moistened considerably at this time. Very little

433 convergence of the meridional flow was present in the vicinity of the equator in the latter half
434 of October, suggesting that the primary contributor to low-level convergence at that time
435 was associated with the zonal flow (to be discussed later). The centroid of heavy rainfall in
436 late October was north of the equator, but the strongest meridional flow was in the opposite
437 hemisphere. This feature is consistent with Hack et al. (1989) and Schubert et al. (1991)
438 who showed that this asymmetric response of the meridional circulation to heating is due
439 to the anisotropy associated with the spatial variation of the inertial stability field, i.e., the
440 low inertial stability in the equatorial region facilitates a stronger meridional circulation on
441 the equator-ward side of the main heated region. Their results assume zonal symmetry, i.e.,
442 no east-west circulations such as those associated with the MJO; however, they might be
443 expected to qualitatively apply to the findings here.

444 A similar shift from a double-ITCZ to a broad rainfall maximum near the equator was
445 seen during the passage of the November MJO (Fig. 17). In this case, the rainfall was fairly
446 evenly distributed across the equator during the active phase, as was the diverging outflow
447 aloft. This result, too, is consistent with Hack et al. (1989), who showed a symmetric response
448 of the upper-level outflow with a heat source on the equator. However, there was an off-
449 equatorial center of maximum convergence of the low-level meridional flow (near 3°N). This
450 feature is likely related to the tropical cyclone activity in the northern hemisphere associated
451 with the November MJO (Fig. 9).

452 5. Diagnosed divergence and vertical motion

453 The evolution of divergence (uncorrected) and vertical motion over the northern sounding
454 array is shown in Fig. 18. Enhanced low-level convergence, upper-level divergence, and
455 upward motion were observed during the active phases of each MJO, although a longer period
456 of deep convection inferred from these fields occurred with the October event. This finding is
457 consistent with the ∼three-week period of mid-tropospheric moistening in October (Fig. 11).

458 Low-level convergence, divergence aloft, and upward vertical motion progressively deepened
459 with time in October, suggesting an evolution from shallow cumulus and congestus to deep
460 convection with this event, as indicated by past studies (Johnson et al. 1999; Kikuchi and
461 Takayabu 2004; Mapes et al. 2006; Yoneyama et al. 2008; Del Genio et al. 2012). A similar
462 progression is seen during the build-up phase in November, but it is briefer, less distinct,
463 and characterized by a more abrupt onset to deep, vigorous upward motion. Consistent with
464 evolution of zonal wind, temperature, and moisture anomalies during the active phases of
465 each MJO (Fig. 11), there is a descent with time of the altitude of the peak upper-level
466 divergence.

467 Time series of divergence and vertical motion for the southern array (Fig. 19) show a
468 distinct contrast with those for the northern array (Fig. 18). Although evidence of enhanced
469 low-level convergence, upper-level divergence, and upward motion occurred in late October
470 and November, there were more frequent periods of upward motion throughout the entire
471 SOP. This behavior is consistent with the time series of relative humidity (Fig. 12) showing
472 frequent periods of moistening, thus reinforcing the picture of quasi-persistent ITCZ
473 conditions south of the equator.

474 As just seen, the evolution of divergence and vertical motion differed significantly between
475 the two arrays. The 1 October-30 November mean profiles of these fields, while broadly
476 similar, also exhibited notable differences (Fig. 20). A deep layer of lower-tropospheric
477 convergence occurred within both arrays with divergence aloft in the 100 to 300 hPa layer.
478 However, the layer of convergence was deeper over the northern array, extending above the
479 0°C level. This feature is possibly an indication of a somewhat higher percentage of stratiform
480 precipitation, and hence melting-layer convergence (Mapes and Houze 1995), north of the
481 equator where the MJO signal was greatest. This supposition is yet to be confirmed by
482 independent measurements, but is consistent with the finding by Lin et al. (2004) of a
483 greater fraction of stratiform rainfall within MJO convection than the global tropical mean.
484 The amplitudes of the mean vertical motion profiles for the two arrays were quite similar,

485 consistent with the approximately equal TRMM-estimated rainfall rates 7.8 and 8.0 mm
486 day⁻¹ for the northern and southern arrays, respectively. However, the vertical motion over
487 the northern array had a distinct peak in the upper troposphere (between 350 and 400 hPa)
488 whereas was the vertical motion over the southern array had a broader peak with a weak
489 maximum near 550 hPa, suggesting differing characteristics of convection between the two
490 domains. The more-elevated peak to the north is also indicative of a higher fraction of
491 stratiform rainfall in that region compared to the south (Houze 1982; Johnson 1984; Houze
492 1989; Schumacher et al. 2004). Further analysis of these differences is underway based on
493 computations of heat and moisture budgets.

494 North-south vertical cross sections of horizontal divergence, relative humidity, and poten-
495 tial temperature from the ECMWF operational analyses, along with TRMM 3B42 rainfall
496 for the first and second halves of October are shown in Fig. 21. The transition from a
497 double-ITCZ structure to a single, broad rain maximum along the equator is accompanied
498 by a similar shift of the low-level convergence/upper-level divergence patterns. The rela-
499 tively shallow low-level convergence layer in the rain bands in early October transitioned to
500 a deep layer of convergence extending to 400 hPa during the latter half of the month. The
501 existence of low-level convergence at and near the equator in the last half of October but
502 with negligible convergence of the meridional flow (Fig. 16), suggests that the primary con-
503 tributor to convergence at this time was in the zonal flow, consistent with the expectations
504 for a Kelvin-Rossby wave response to an equatorial heat source Gill (1980).

505 A similar transition occurred from the first to the second half of November when there
506 was a shift from a double-ITCZ pattern to a broad rainfall maximum along the equator (Fig.
507 22). A deeper layer of lower-tropospheric convergence occurred in the latter half of November
508 along with stronger, more-elevated peaks in upper-level divergence. A convergence maximum
509 near 500 hPa in late November is once again suggestive of melting-layer effects in association
510 with stratiform precipitation during the active phase of the MJO. Both the mean divergence
511 profiles based on sounding data only (Fig. 20) and those from the ECMWF analysis (Figs. 21

512 and 22) indicate a slightly higher level of the peak in upper-level divergence over the northern
513 array than the southern array. This behavior could be related to the slightly higher average
514 SSTs over the northern array (Fig. 4) during the SOP and/or the predominance of the MJO
515 signal to the north accompanied by more organized convection.

516 Vertical cross sections of vertical motion for the first and last halves of November are
517 presented in Fig. 23. Over this period, there is a shift in the level of the peak upward motion
518 from the low-to-midtroposphere to the mid-to-upper troposphere. The higher peak during
519 late November is consistent with the earlier inference of a higher percentage of stratiform
520 precipitation during the active phase of the MJO. A similar broadening, intensification, and
521 high-level peak (near 400 hPa) in upward motion occurred during the late-October active
522 phase of the MJO (not shown).

523 6. Summary and conclusions

524 Sounding data from two quadrilateral arrays, one north and one south of the equator,
525 have been used to diagnose the kinematic and thermodynamic properties and structure of
526 the October and November 2011 MJO events during the DYNAMO field campaign over the
527 Indian Ocean. The analyses for the sounding arrays are based on a preliminary version of
528 the quality-controlled, high-resolution sounding data set. Efforts to complete quality control
529 of the data, e.g., corrections for sonde humidity biases, are ongoing.

530 The principal findings with respect to the broad-scale conditions during the DYNAMO
531 Special Observing Period over the Indian Ocean are:

- 532 • DYNAMO occurred during a La Niña and near-neutral Indian Ocean Dipole conditions
533 such that positive SST anomalies existed over much of the Indian Ocean; correspond-
534 ingly, slightly above-normal precipitation occurred over much of the Indian Ocean.
- 535 • Heaviest precipitation over the Indian Ocean occurred in east-west bands north and

536 south of the equator in proximity to the strongest SST gradients.

537 With respect to the evolution of the winds, vertical motion, thermodynamic fields, SST,
538 and precipitation during the passage of the two MJOs, the primary findings are summarized
539 in Fig. 24. The northern array experienced the strongest MJO signal, so this schematic
540 depiction refers to results for that domain. Specifically, precipitation over the northern
541 sounding array was strongly modulated by the MJOs; the southern array experienced more
542 persistent, briefer episodes of precipitation mostly related to ITCZ convection.

- 543 • The development of the October MJO over the northern sounding array was charac-
544 terized by gradual moistening of the low-to-mid-troposphere over a \sim two-week period
545 during which multiple westward-moving, two-day disturbances affected the region, sim-
546 ilar to the December 1992 MJO during TOGA COARE (Takayabu et al. 1996; Haertel
547 and Johnson 1998).
- 548 • The November MJO exhibited a similar \sim two-week period of a build-up of low-to-
549 midlevel moisture preceding the convectively active phase, which was dominated by
550 two strong Kelvin waves each with diagnosed intense upward motion.
- 551 • Low-level westerly flow preceded the October MJO; low-level easterlies preceded the
552 second MJO.
- 553 • Patterns of relative humidity, divergence and vertical motion support the concept of
554 shallow cumulus-to-congestus-to-deep convection evolution of the cloud population in a
555 stepwise manner, consistent with past studies (Kikuchi and Takayabu 2004; Yoneyama
556 et al. 2008; Del Genio et al. 2012).
- 557 • Thermal anomalies in the low-to-mid-troposphere within the MJO convective envelope
558 – cool anomalies at low levels and warm anomalies in the upper troposphere – are
559 consistent with findings from past studies (Lin and Johnson 1996; Kiladis et al. 2005).

- Tilted cool/warm and zonal wind anomalies occurred for extended periods (multiple weeks) in the upper troposphere and lower stratosphere, reflecting gravity or Kelvin waves excited by the MJO convective envelopes (Kiladis et al. 2001; Virts and Wallace 2010; Virts et al. 2010); the temperature anomalies contributed to sharp jumps in the cold-point tropopause level at the end of the heavy rainfall periods.
- The cool-anomaly portions of these upper-level features had associated positive moisture anomalies aloft that arrived several weeks prior to the heaviest rain periods of the MJOs.
- The quiescent period of the MJOs were characterized by gradual SST rises with accompanying distinct diurnal cycles, while the active phases exhibited falling SSTs with a damped diurnal cycle as also found during TOGA COARE (Webster et al. 1996; Weller and Anderson 1996).

While there are a number of similarities in the characteristics of the two MJOs, there are sufficient differences to warrant caution in generalizing results from these events. In particular, we attempted the creation of a composite of the two cases by RMM phase, but it led to unrealistic features that were not representative of the individual events themselves.

This study has only explored the gross features of the October and November MJOs observed during DYNAMO. Many details have yet to be investigated, particularly the processes leading to moistening of the lower troposphere prior to deep convection. That effort will require an integration of the results from the sounding array with other DYNAMO/CINDY/AMIE observations, especially the evolving cloud and precipitation fields as determined by radars and lidars.

Acknowledgments.

The success of the DYNAMO/CINDY/AMIE sounding campaign is a result of the substantial contributions and dedication of many individuals, including students and other staff

585 from the United States, Taiwan, and Japan who helped with the operations at the various
586 sounding sites. We thank Eric DeWeaver and Brad Smull of the National Science Founda-
587 tion for supporting the sounding installation at Malé. We also thank Bill Brown, Masaki
588 Katsumata, Scot Loehrer, Chuck Long, Jim Moore, June Wang, Steve Williams, Kunio
589 Yoneyama, and Kate Young for assistance with both the field phase and post-field phase
590 sounding data support and processing. SST data from the *Revelle* were provided by James
591 Edson, Chris Fairall, and Simon de Szoek. The help of Rick Taft and Kathy Straub with
592 figures is greatly appreciated. We thank Chidong Zhang for valuable interactions through-
593 out the campaign and Paul Roundy and two anonymous reviewers for helpful reviews of the
594 manuscript. This research has been supported by the National Science Foundation under
595 Grants AGS-1059899 and AGS-1138353.

REFERENCES

- 598 Benedict, J. and D. A. Randall, 2007: Observed characteristics of the MJO relative to
 599 maximum rainfall. *J. Atmos. Sci.*, **64**, 2332–2354.
- 600 Benedict, J. and D. A. Randall, 2009: Structure of the Madden-Julian Oscillation in the
 601 Superparameterized CAM. *J. Atmos. Sci.*, **66**, 3277–3296.
- 602 Bladé, I. and D. L. Hartmann, 1993: Tropical intraseasonal oscillation in a simple nonlinear
 603 model. *J. Atmos. Sci.*, **50**, 2922–2939.
- 604 Chen, S. S., R. A. Houze, Jr., and B. E. Mapes, 1996: Multiscale variability of deep convec-
 605 tion in relation to large-scale circulation in TOGA COARE. *J. Atmos. Sci.*, **53**, 1380–1409.
- 606 Ciesielski, P. E., L. Hartten, and R. H. Johnson, 1997: Impacts of merging profiler and
 607 rawinsonde winds on TOGA COARE analyses. *J. Atmos. Oceanic Technol.*, **14**, 1264–
 608 1279.
- 609 Ciesielski, P. E., R. H. Johnson, P. T. Haertel, and J. Wang, 2003: Corrected TOGA COARE
 610 sounding humidity data: Impact on diagnosed properties of convection and climate over
 611 the warm pool. *J. Climate*, **16**, 2370–2384.
- 612 Ciesielski, P. E., et al., 2010: Quality controlled upper-air sounding dataset for TiM-
 613 REX/SoWMEX: Development and corrections. *J. Atmos. Oceanic Technol.*, **27**, 1802–
 614 1821.
- 615 Cronin, M. F. and M. J. McPhaden, 1997: Diurnal variation and lifecycle of deep convective
 616 systems over the tropical Pacific warm pool. *J. Geophys. Res.*, **102**, 8533–8553.

- 617 Del Genio, A. D., Y. Chen, D. Kim, and M.-S. Yao, 2012: The MJO transition from shallow
618 to deep convection in *cloudsat/CALIPSO* and GISS GCM simulations. *J. Climate*, **25**,
619 3755–3770.
- 620 Flatau, M., P. J. Flatau, P. Phoebus, and P. P. Niiler, 1997: The feedback between equatorial
621 convection and local radiative and evaporative processes: The implication for intraseasonal
622 oscillations. *J. Atmos. Sci.*, **54**, 2373–2386.
- 623 Gill, A. E., 1980: Some simple solutions for heat-induced tropical circulation. *Quart. J. Roy.*
624 *Meteor. Soc.*, **106**, 447–462.
- 625 Godfrey, J. S., R. A. Houze, Jr., R. H. Johnson, R. Lukas, J.-L. Redelsperger, A. Sui, and
626 R. Weller, 1998: Coupled Ocean-Atmosphere Response Experiment: An interim report.
627 *J. Geophys. Res.*, **103**, 14 395–14 450.
- 628 Hack, J. J., W. H. Schubert, D. E. Stevens, and H.-C. Kuo, 1989: Response of the Hadley
629 Circulation to convective forcing in the ITCZ. *J. Atmos. Sci.*, **46**, 2957–2973.
- 630 Haertel, P. T. and R. H. Johnson, 1998: Two-day disturbances in the equatorial western
631 Pacific. *Quart. J. Roy. Meteor. Soc.*, **124**, 615–636.
- 632 Haertel, P. T., G. N. Kiladis, A. Denno, and T. M. Rickenbach, 2008: Vertical-mode decom-
633 positions of 2-day waves and the Madden-Julian Oscillation. *J. Atmos. Sci.*, **65**, 813–833.
- 634 Hermes, J. C. and C. J. C. Reason, 2008: Annual cycle of the South Indian Ocean (Seychelles-
635 Chagos) thermocline ridge in a regional ocean model. *J. Geophys. Res.*, **31**, doi:10.1029/
636 2004GL019601.
- 637 Hohenegger, C. and B. Stevens, 2013: Preconditioning deep convection with cumulus con-
638 gestus. *J. Atmos. Sci.*, **70**, 448–464.
- 639 Houze, R. A., Jr., 1982: Cloud clusters and large-scale vertical motion in the tropics. *J.*
640 *Meteor. Soc. Japan*, **60**, 396–410.

- 641 Houze, R. A., Jr., 1989: Observed structure of mesoscale convective systems and implications
642 for large-scale heating. *Quart. J. Roy. Meteor. Soc.*, **115**, 425–461.
- 643 Hu, Q. and D. A. Randall, 1994: Low-frequency oscillations in radiative-convective systems.
644 *J. Atmos. Sci.*, **51**, 1089–1099.
- 645 Huffman, G. J., R. F. Adler, D. T. Bolvin, G. Gu, E. J. Nelkin, K. P. Bowman, E. F.
646 Stocker, and D. B. Wolff, 2007: The TRMM multi-satellite precipitation analysis: Quasi-
647 global, multi-year, combined-sensor precipitation estimates at fine scale. *J. Hydrometeor.*,
648 **8**, 33–55.
- 649 Hung, M.-P., J.-L. Lin, W. Wang, D. Kim, T. Shinoda, and S. J. Weaver, 2013: MJO and
650 convectively coupled equatorial waves simulated by CMIP5 climate models. *J. Climate*,
651 (in press).
- 652 Johnson, R. H., 1984: Partitioning tropical heat and moisture budgets into cumulus and
653 mesoscale components: Implications for cumulus parameterization. *Mon. Wea. Rev.*, **112**,
654 1590–1601.
- 655 Johnson, R. H. and P. E. Ciesielski, 2002: Characteristics of the 1998 summer monsoon
656 onset over the northern South China Sea. *J. Meteor. Soc. Japan*, **80**, 561–578.
- 657 Johnson, R. H. and X. Lin, 1987: Episodic trade wind regimes over the western Pacific warm
658 pool. *J. Atmos. Sci.*, **54**, 2020–2034.
- 659 Johnson, R. H., T. M. Rickenbach, S. A. Rutledge, P. E. Ciesielski, and W. H. Schubert,
660 1999: Trimodal characteristics of tropical convection. *J. Atmos. Sci.*, **58**, 2729–2750.
- 661 Kalnay, E., et al., 1996: The NCEP/NCAR 40-year reanalysis project. *Bull. Amer. Meteor.
662 Soc.*, **77**, 437–470.
- 663 Katsumata, M., P. E. Ciesielski, and R. H. Johnson, 2011: Evaluation of budget analysis
664 during MISMO. *J. Appl. Meteor. Climatol.*, **40**, 241–254.

- 665 Kemball-Cook, S. R. and B. C. Weare, 2001: The onset of convection in the Madden-Julian
666 Oscillation. *J. Climate*, **14**, 780–793.
- 667 Kikuchi, K. and Y. N. Takayabu, 2004: The development of organized convection associated
668 with the MJO during TOGA COARE IOP: Trimodal characteristics. *Geophys. Res. Lett.*,
669 **31**, doi:10.1029/2004GL019601.
- 670 Kiladis, G. N., K. H. Straub, and P. T. Haertel, 2005: Zonal and vertical structure of the
671 Madden-Julian oscillation. *J. Atmos. Sci.*, **62**, 2790–2809.
- 672 Kiladis, G. N., K. H. Straub, G. C. Reid, and K. S. Gage, 2001: Aspects of interannual and
673 intraseasonal variability of the tropopause and lower stratosphere. *Quart. J. Roy. Meteor.
674 Soc.*, **127**, 1961–1984.
- 675 Kim, H.-M., C. D. Hoyos, P. J. Webster, and I. S. Kang, 2009: Ocean-atmosphere coupling
676 and the boreal winter MJO. *Clim. Dynam.*, doi:10.1007/s00382-009-0612-x.
- 677 Lau, W. K. M. and D. E. Waliser, 2005: *Intraseasonal variability of the atmosphere-ocean
678 climate system*. Springer, 474 pp.
- 679 Liebmann, B. and C. A. Smith, 1996: Description of a complete (interpolated) outgoing
680 longwave radiation dataset. *Bull. Amer. Meteor. Soc.*, **77**, 1275–1277.
- 681 Lin, J.-L., B. E. Mapes, M. Zhang, and N. Newman, 2004: Stratiform precipitation, vertical
682 heating profiles, and the Madden-Julian Oscillation. *J. Atmos. Sci.*, **61**, 296–309.
- 683 Lin, J.-L., et al., 2006: Tropical intraseasonal variability in 14 ipcc ar4 climate models. part
684 i: Convective signals. *J. Climate*, **19**, 2665–2690.
- 685 Lin, X. and R. H. Johnson, 1996: Kinematic and thermodynamic characteristics of the flow
686 over the western Pacific warm pool during TOGA COARE. *J. Atmos. Sci.*, **53**, 695–715.
- 687 Lukas, R. and E. Lindstrom, 1991: The mixed layer of the western equatorial Pacific Ocean.
688 *J. Geophys. Res.*, **96**, 3343–3357.

- 689 Madden, R. A. and P. R. Julian, 1972: Description of global-scale circulation cells in the
690 tropics with a 40-50 day period. *J. Atmos. Sci.*, **29**, 1109–1123.
- 691 Maloney, E. D., 2009: The moist static energy budget of a composite tropical intraseasonal
692 oscillation in a climate model. *J. Climate*, **22**, 711–729.
- 693 Maloney, E. D. and D. L. Hartmann, 1998: Frictional moisture convergence in a composite
694 life cycle of the Madden-Julian Oscillation. *J. Climate*, **11**, 2387–2403.
- 695 Mapes, B. E. and R. A. Houze, Jr., 1995: Diabatic divergence profiles in western Pacific
696 mesoscale convective systems. *J. Atmos. Sci.*, **52**, 1807–1828.
- 697 Mapes, B. E., S. Tulich, J. Lin, and P. Zuidema, 2006: The mesoscale convection life cycle:
698 Building block or prototype for large-scale tropical waves? *Dyn. Atmos. Oceans*, **42**, 3–29.
- 699 Matthews, A. J., 2008: Primary and successive events in the Madden-Julian Oscillation.
700 *Quart. J. Roy. Meteor. Soc.*, **134**, 439–453.
- 701 Meyers, G., P. McIntosh, L. Pigot, and M. Pook, 2007: The years of El Niño, La Niña, and
702 interactions with the tropical Indian Ocean. *J. Climate*, **20**, 2872–2880.
- 703 Mori, S., et al., 2004: Diurnal land-sea rainfall peak migration over Sumatera Island, Indone-
704 sian maritime continent observed by TRMM satellite and intensive rawinsonde soundings.
705 *Mon. Wea. Rev.*, **132**, 2021–2039.
- 706 Nakazawa, T., 1988: Tropical super clusters within intraseasonal variations over the western
707 pacific. *J. Meteor. Soc. Japan*, **66**, 823–839.
- 708 Reynolds, R. W., T. M. Smith, C. Liu, D. B. Chelton, K. S. Casey, and M. G. Schlax,
709 2007: Daily high-resolution-blended analyses for sea surface temperature. *J. Climate*, **20**,
710 5473–5496.
- 711 Riley, E. M., B. E. Mapes, and S. N. Tulich, 2011: Clouds associated with the Madden-Julian
712 oscillation: A new perspective from *cloudsat*. *J. Atmos. Sci.*, **68**, 3032–3051.

- 713 Roundy, P. E., 2012a: Observed structure of convectively coupled waves as a function of
714 equivalent depth: Kelvin waves and the Madden-Julian Oscillation. *J. Atmos. Sci.*, **69**,
715 2097–2106.
- 716 Roundy, P. E., 2012b: The spectrum of convectively coupled Kelvin waves and the Madden-
717 Julian Oscillation in regions of low-level easterly and westerly background flow. *J. Atmos.*
718 *Sci.*, **69**, 2107–2111.
- 719 Roundy, P. E. and L. M. Gribble-Verhagen, 2010: Variations in the flow of the global
720 atmosphere associated with a composite convectively coupled oceanic Kelvin wave. *J.*
721 *Climate*, **23**, 4192–4201.
- 722 Roundy, P. E., C. J. Schreck, and M. A. Janiga, 2009: Contributions of convectively coupled
723 equatorial Rossby waves and Kelvin waves to the Real-time Multivariate MJO indices.
724 *Mon. Wea. Rev.*, **137**, 469–478.
- 725 Sakurai, N., et al., 2005: Diurnal cycle of cloud system migration over Sumatera Island. *J.*
726 *Meteor. Soc. Japan*, **83**, 835–850.
- 727 Schubert, W. H., P. E. Ciesielski, D. E. Stevens, and H.-C. Kuo, 1991: Potential vorticity
728 modeling of the ITCZ and the Hadley Circulation. *J. Atmos. Sci.*, **48**, 1493–1509.
- 729 Schumacher, C., R. A. Houze, Jr., and I. Kraucunas, 2004: The tropical dynamical response
730 to latent heating estimates derived from the trmm precipitation radar. *J. Atmos. Sci.*, **61**,
731 1341–1358.
- 732 Shinoda, T. and H. H. Hendon, 1998: Mixed layer modeling of intraseasonal variability in
733 the tropical western Pacific and Indian Oceans. *J. Climate*, **11**, 2668–2685.
- 734 Small, R. J., et al., 2008: Air-sea interaction over ocean fronts and eddies. *Dyn. Atmos.*
735 *Oceans*, **45**, 274–319.

- 736 Stephens, G. L., P. J. Webster, R. H. Johnson, R. Engelen, and T. S. L'Ecuyer, 2004:
737 Observational evidence for the mutual regulation of the tropical hydrological cycle and
738 the tropical sea surface temperatures. *J. Climate*, **17**, 2213–2224.
- 739 Straub, K. H., 2013: MJO initiation in the Real-Time Multivariate MJO Index. *J. Climate*,
740 **26**, 1130–1151.
- 741 Straub, K. H. and G. N. Kiladis, 2002: Observations of a convectively coupled Kelvin wave
742 in the eastern Pacific ITCZ. *J. Atmos. Sci.*, **59**, 30–53.
- 743 Takayabu, Y. N., K.-M. Lau, and C.-H. Sui, 1996: Observation of a quasi-2-day wave during
744 TOGA COARE. *Mon. Wea. Rev.*, **124**, 1892–1913.
- 745 Tam, C.-Y. and N.-C. Lau, 2005: Modulation of the Madden-Julian Oscillation by ENSO:
746 Inference from observations and GCM simulations. *J. Meteor. Soc. Japan*, **83**, 727–743.
- 747 Vialard, J., et al., 2009: Air-sea interactions in the Seychelles-Chagos Thermocline Ridge
748 region. *Bull. Amer. Meteor. Soc.*, **90**, 45–61.
- 749 Virts, K. S. and J. M. Wallace, 2010: Annual, interannual, and intraseasonal variability of
750 tropical tropopause transition layer cirrus. *J. Atmos. Sci.*, **67**, 3113–3129.
- 751 Virts, K. S., J. M. Wallace, Q. Fu, and T. P. Ackerman, 2010: Tropical tropopause transition
752 layer cirrus as represented by calipso lidar observations. *J. Atmos. Sci.*, **67**, 3097–3112.
- 753 Waite, M. L. and B. Khouider, 2010: The deepening of tropical convection by congestus
754 preconditioning. *J. Atmos. Sci.*, **67**, 2601–2615.
- 755 Waliser, D. E., 2006: Intraseasonal variability. *The Asian Monsoon*, B. Wang, Ed., Springer,
756 203–257.
- 757 Wang, B., 2005: Theory. *Intraseasonal variability in the atmosphere-ocean climate system*,
758 W. K. M. Lau and D. E. Waliser, Eds., Springer, 19–61.

- 759 Wang, J., H. L. Cole, D. J. Carlson, E. R. Miller, K. Beierle, A. Paukkunen, and T. K. Laine,
760 2002: Corrections of the humidity measurement errors from the vaisala rs80 radiosonde—
761 Application to TOGA COARE data. *J. Atmos. Oceanic Technol.*, **19**, 981–1002.
- 762 Wang, J. and L. Zhang, 2008: Systematic errors in global radiosonde precipitable water data
763 from comparisons with ground-based GPS measurements. *J. Climate*, **21**, 2218–2238.
- 764 Wang, J., L. Zhang, A. Dai, F. Immler, and H. Vömel, 2013: Radiation dry bias correction
765 of Vaisala RS92 humidity data and its impact on historical radiosonde data. *J. Atmos.*
766 *Oceanic Technol.*, (in press).
- 767 Webster, P. J., C. A. Clayson, and J. A. Curry, 1996: Clouds, radiation and the diurnal cycle
768 of sea surface temperature in the tropical western Pacific Ocean. *J. Climate*, **9**, 1712–1730.
- 769 Webster, P. J., A. Moore, J. Loschnigg, and M. Leban, 1999: Coupled ocean-atmosphere
770 dynamics in the Indian Ocean during 1997-98. *Nature*, **401**, 356–360.
- 771 Weller, R. A. and S. P. Anderson, 1996: Surface meteorology and air-sea fluxes in the western
772 equatorial Pacific warm pool during the TOGA Coupled Ocean-Atmosphere Response
773 Experiment. *J. Climate*, **9**, 1959–1990.
- 774 Wheeler, M. C. and H. H. Hendon, 2004: An all-season real-time multivariate MJO index:
775 Development of an index for monitoring and prediction. *Mon. Wea. Rev.*, **132**, 1917–1932.
- 776 Wheeler, M. C. and K. M. Weickmann, 2001: Real-time monitoring and prediction of modes
777 of coherent synoptic to intraseasonal tropical variability. *Mon. Wea. Rev.*, **129**, 2677–2694.
- 778 Xie, S.-P., 2004: Satellite observations of cool oceanatmosphere interaction. *Bull. Amer.*
779 *Meteor. Soc.*, **85**, 195–208.
- 780 Yamada, H., K. Yoneyama, M. Katsumata, and R. Shirooka, 2010: Observations of a super
781 cloud cluster accompanied by synoptic-scale eastward-propagating precipitating systems
782 over the Indian Ocean. *J. Atmos. Sci.*, **67**, 1456–1473.

- 783 Yoneyama, K., C. Zhang, and C. N. Long, 2013: Tracking pulses of the Madden-Julian
784 Oscillation. *Bull. Amer. Meteor. Soc.*, (in press).
- 785 Yoneyama, K., et al., 2008: MISMO field experiment in the equatorial Indian Ocean. *Bull.*
786 *Amer. Meteor. Soc.*, **89**, 1889–1903.
- 787 Yu, L. and R. A. Weller, 2007: Objectively analyzed air-sea heat fluxes for the global oceans
788 (1981-2005). *Bull. Amer. Meteor. Soc.*, **88**, 527–539.
- 789 Yuan, J. and R. A. Houze, Jr., 2013: Deep convective systems observed by A-Train in the
790 tropical Indo-Pacific region affected by the MJO. *J. Atmos. Sci.*, **70**, 465–486.
- 791 Zhang, C., 2005: Madden-Julian Oscillation. *Rev. Geophys.*, **89**, 2003, doi:10.1029/
792 2004RG000158.
- 793 Zhang, C., J. Gottschalck, E. D. Maloney, M. W. Moncrieff, F. Vitart, D. E. Waliser,
794 B. Wang, and M. C. Wheeler, 2013: Cracking the MJO nut. *Geophys. Res. Lett.*, **40**,
795 1223–1230, doi:10.1002/grl.50244,2013.

796 List of Tables

- 797 1 Sounding sites comprising quadrilateral arrays for the Special Observing Pe-
798 riod (SOP; 1 October – 15 December 2011). Ship locations are nominal posi-
799 tions; they neglect minor on-station maneuvering and port calls. 34

TABLE 1. Sounding sites comprising quadrilateral arrays for the Special Observing Period (SOP; 1 October – 15 December 2011). Ship locations are nominal positions; they neglect minor on-station maneuvering and port calls.

Station	Location	Elevation (m)	Instrument type	No. SOP soundings
Gan Island	0.69 S 73.15 E	01	Vaisala RS92	620
R/V <i>Revelle</i>	0.00 N 80.50 E	19	Vaisala RS92	444
Diego Garcia	7.31 S 72.43 E	02	Vaisala RS92	513
R/V <i>Mirai</i>	8.00 S 80.50 E	18	Vaisala RS92	485
Malé	4.19 N 73.53 E	02	Vaisala RS92	320
Colombo	6.91 N 79.87 E	15	Meisei RS06G	255

800 List of Figures

- 801 1 DYNAMO/CINDY/AMIE sounding network for the period October-December
802 2011. Analysis domain includes high-frequency soundings (4 and 8 per day;
803 yellow and red dots, respectively) and priority sounding sites (1 or 2 per day;
804 black dots). Data from R/V *Sagar Kanya* (*S. K.*) and R/V *Baruna Jaya* (*B.*
805 *J.*), which were on station for brief periods (25 September-19 October for *S.*
806 *K.* and 5-18 December for *B. J.*), were also utilized in the analyses. 40
- 807 2 Sea surface temperature anomalies (C) from the long-term (1981-2012) mean
808 over tropical Pacific and Indian Oceans during the DYNAMO period 1 Oc-
809 tober – 15 December 2011 based on Reynolds et al. (2007) high-resolution
810 blended analysis. 41
- 811 3 (a) TRMM 3B42 precipitation (mm day^{-1}) and ECMWF operational analysis
812 surface streamlines, and (b) TRMM 3B42 precipitation anomalies (mm day^{-1})
813 and NCEP/NCAR reanalysis 500-hPa vertical p -velocity anomalies (hPa h^{-1})
814 for the DYNAMO period 1 October – 15 December 2011. Anomalies are
815 computed from a 14-year (1998-2011) mean corresponding to the period of
816 the TRMM satellite. Polygons indicate the two DYNAMO sounding arrays. 42
- 817 4 TRMM 3B42 precipitation (mm day^{-1}) and OAFlux SST (C) for the DY-
818 NAMO period 1 October – 15 December 2011. Polygons indicate the two
819 DYNAMO sounding arrays. 43
- 820 5 Time series (from top to bottom) of hourly sea-surface temperature ($^{\circ}\text{C}$) at
821 1.5-m depth for DYNAMO SOP based on data from the RAMA buoy at 1.5°S
822 90°E , time series of 3-hourly average TRMM 3B42 rainfall (mm h^{-1}) within
823 a 1° radius of same buoy, hourly wind speed (m s^{-1}) at same buoy, and time
824 series of daily-averaged sea level pressure (hPa) at RAMA buoy at equator
825 and 80.5°E . 44

- 826 6 Wheeler and Hendon (2004) Real-time Multivariate MJO (RMM) Index for
 827 period 1 October-15 December 2011 illustrating global progression and am-
 828 plitude of October and November MJOs. 45
- 829 7 Time-latitude plot of Outgoing Longwave Radiation (OLR) anomalies (W m^{-2}) computed from 1981-2010 long-term mean from 20°N to 20°S averaged
 830 from 60 to 90°E for period 1 October 2011-31 March 2012. Approximate sea-
 831 sonal track of anomaly centroid centers is indicated. October and November
 832 MJO active phases are denoted. 46
- 833 8 Time-latitude plot of TRMM 3B42 precipitation (mm day^{-1}) from 15°N to
 834 15°S averaged from 72 to 80°E for the period 1 October-15 December 2011.
 835 Latitudinal extents of northern and southern sounding arrays are indicated. 47
- 836 9 Meteosat thermal IR image for 1200 UTC 25 November 2011. The tropical
 837 depression near the south tip of India became Tropical Storm 05A on 26
 838 November. 48
- 839 10 Time-longitude plot of TRMM 3B42 precipitation (mm day^{-1}) and ECMWF
 840 500-hPa vertical p -velocity (hPa h^{-1}) from 35° to 155°E averaged from 5°N
 841 to 5°S for the period 1 October-15 December 2011. Heavy solid line is zero
 842 contour; dashed contours indicate upward motion with contour interval of 10
 843 hPa h^{-1} . Vertical dashed line denotes center of DYNAMO sounding arrays. 49
- 844 11 Time series over northern sounding array (from top to bottom) of zonal wind
 845 (m s^{-1}), relative humidity (%; with respect to ice for $T < 0^\circ\text{C}$), temperature
 846 anomaly ($^\circ\text{C}$), and daily-averaged TRMM 3B42 rainfall (mm day^{-1}). Winds
 847 and thermodynamics are based on daily averages of six-hourly soundings,
 848 with temperature anomaly based on SOP mean. Color bars at bottom refer
 849 to phases of RMM index shown in Fig. 6. Vertical shaded bars indicate times
 850 when R/V *Revelle* was off station. 50

- 852 12 As in Fig. 11, except for southern sounding array. Dark and light vertical
853 shaded bars indicate times when R/V *Mirai* and *Revelle*, respectively, were
854 off station. 51

855 13 Time series of relative humidity (%), with respect to ice for $T < 0^\circ\text{C}$) from 1
856 October to 15 December at Malé, Gan Island, R/V *Revelle*, and Diego Garcia
857 based on full time resolution of sounding data. See Fig. 1 for site locations.
858 Dotted line segments denote approximate tops of moist layers. Thin white
859 line denotes 0°C level. 52

860 14 (top) Two-month (1 October-30 November) mean vertical profiles of zonal and
861 meridional wind (m s^{-1}), equivalent potential temperature (K), and relative
862 humidity (with respect to ice for $T < 0^\circ\text{C}$), and (bottom) standard deviations
863 of these variables for the northern (solid) and southern (dashed) sounding
864 arrays. 53

865 15 Mean, pre-active, and active phase profiles of (left) zonal wind (m s^{-1}) and
866 (right) relative humidity (%; with respect to ice for $T < 0^\circ\text{C}$) for (top) October
867 and (bottom) November. Pre-active and active dates are 5 and 26 for October
868 and 16 and 27 for November. 54

869 16 North-south cross section through sounding arrays of ECMWF operational
870 analysis (top) relative humidity (%), with respect to ice for $T < 0^\circ\text{C}$) and
871 meridional wind (contour interval: 1 m s^{-1}), and (bottom) TRMM 3B42
872 rainfall for periods (left) 1-15 October and (right) 16-31 October 2011. 55

873 17 As in Fig. 16, except for periods (left) 1-15 November and (right) 16-30 Novem-
874 ber 2011. 56

875 18 SOP time series of (top) TRMM 3B42 rainfall, (middle) uncorrected diver-
876 gence (10^{-6} s^{-1}), and (bottom) vertical motion (hPa h^{-1}) for northern sound-
877 ing array. Color bars at bottom refer to phases of RMM index shown in Fig.
878 6. Vertical shaded bars indicate times when R/V *Revelle* was off station. 57

879 19 As in Fig. 18, but for southern array. Dark and light vertical shaded bars
880 indicate times when R/V *Mirai* and *Revelle*, respectively, were off station. 58

881 20 1 October-30 November mean vertical profiles of divergence (10^{-6} s^{-1}) and
882 vertical motion (hPa h^{-1}) for the northern (solid) and southern (dashed)
883 sounding arrays. 59

884 21 North-south cross section through sounding arrays of ECMWF operational
885 analysis (top) relative humidity (%), with respect to ice for $T < 0^\circ\text{C}$, hori-
886 zontal divergence (contour interval: $2 \times 10^{-6} \text{ s}^{-1}$), and potential temperature
887 (K, thin quasi-horizontal lines; contour interval: 5 K); and (bottom) TRMM
888 3B42 rainfall for periods (left) 1-15 October and (right) 16-31 October 2011. 60

889 22 As in Fig. 21, except for periods (left) 1-15 November and (right) 16-30 Novem-
890 ber 2011. 61

891 23 North-south cross section through sounding arrays of ECMWF operational
892 analysis (top) relative humidity (%), with respect to ice for $T < 0^\circ\text{C}$, vertical
893 motion (contour interval: 1 hPa h^{-1}), and potential temperature (K, thin
894 quasi-horizontal lines); and (bottom) TRMM 3B42 rainfall for periods (left)
895 1-15 November and (right) 16-30 November 2011. 62

896 24 (top panel) Integrated depiction of vertical structure of two MJOs during the
897 period 1 October-15 December 2011 based on mean fields over northern sound-
898 ing array. Green (yellow) shading denotes areas of relative humidity $> 70\%$
899 ($< 40\%$), respectively. Thin (broad) arrows denote locations of zonal wind
900 (vertical motion) maxima. Centers of cool and warm temperature anom-
901 alies are shown. Relative magnitudes of features are represented by sizes of
902 symbols. At upper levels, these anomalies have a tilted structure as do the
903 easterly wind maxima. Daily-averaged 0°C level (dashed line) and cold-point
904 tropopause level (solid line) are indicated. (middle panel) Hourly SST time
905 series at R/V *Revelle*. (bottom panel) TRMM 3B42 daily-averaged rainfall
906 rate over the northern sounding array.

63

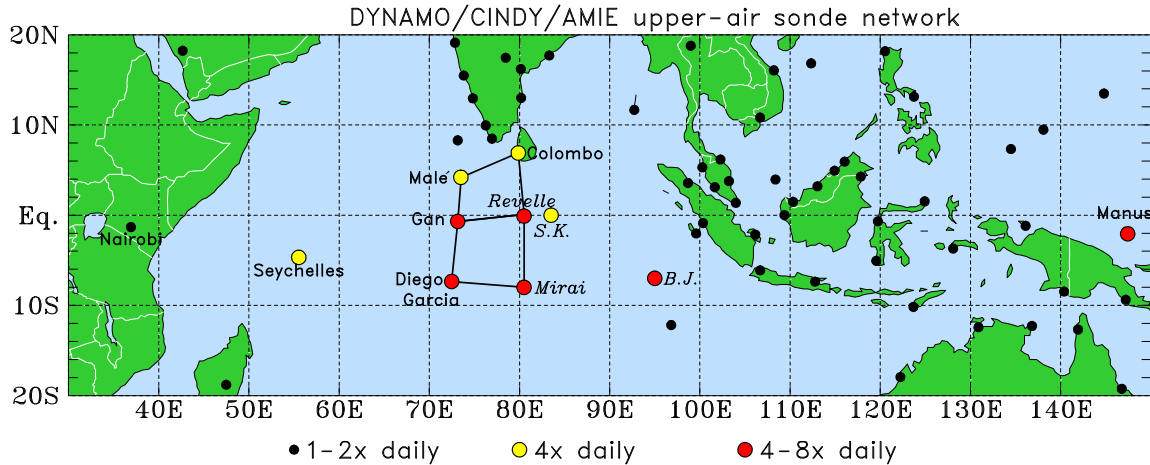


FIG. 1. DYNAMO/CINDY/AMIE sounding network for the period October–December 2011. Analysis domain includes high-frequency soundings (4 and 8 per day; yellow and red dots, respectively) and priority sounding sites (1 or 2 per day; black dots). Data from R/V *Sagar Kanya* (*S. K.*) and R/V *Baruna Jaya* (*B. J.*), which were on station for brief periods (25 September–19 October for *S. K.* and 5–18 December for *B. J.*), were also utilized in the analyses.

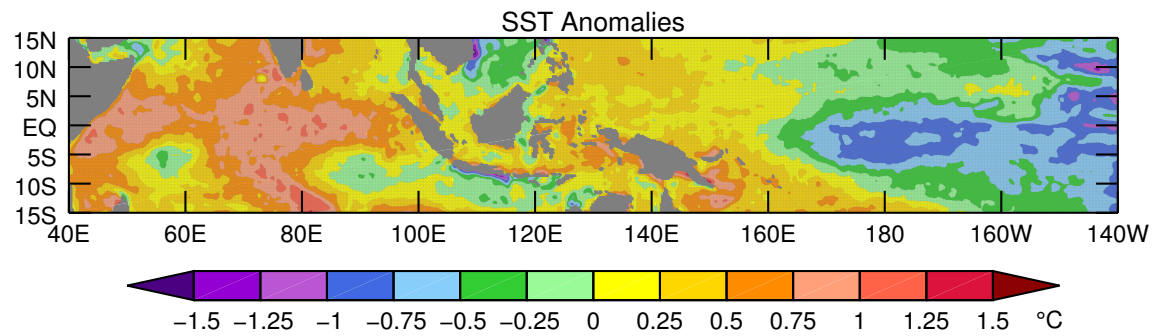


FIG. 2. Sea surface temperature anomalies (C) from the long-term (1981-2012) mean over tropical Pacific and Indian Oceans during the DYNAMO period 1 October – 15 December 2011 based on Reynolds et al. (2007) high-resolution blended analysis.

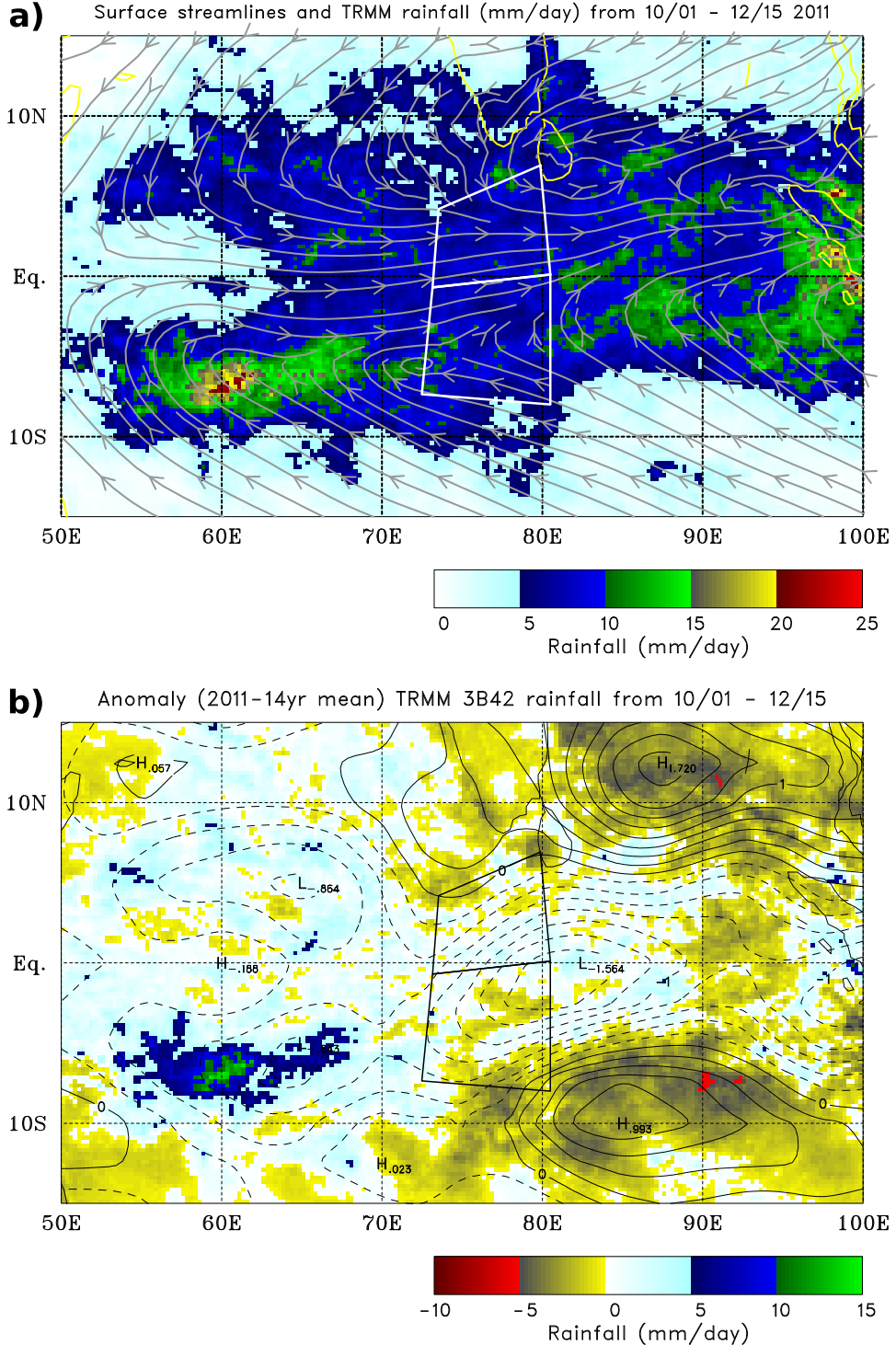


FIG. 3. (a) TRMM 3B42 precipitation (mm day^{-1}) and ECMWF operational analysis surface streamlines, and (b) TRMM 3B42 precipitation anomalies (mm day^{-1}) and NCEP/NCAR reanalysis 500-hPa vertical p -velocity anomalies (hPa h^{-1}) for the DYNAMO period 1 October – 15 December 2011. Anomalies are computed from a 14-year (1998–2011) mean corresponding to the period of the TRMM satellite. Polygons indicate the two DYNAMO sounding arrays.

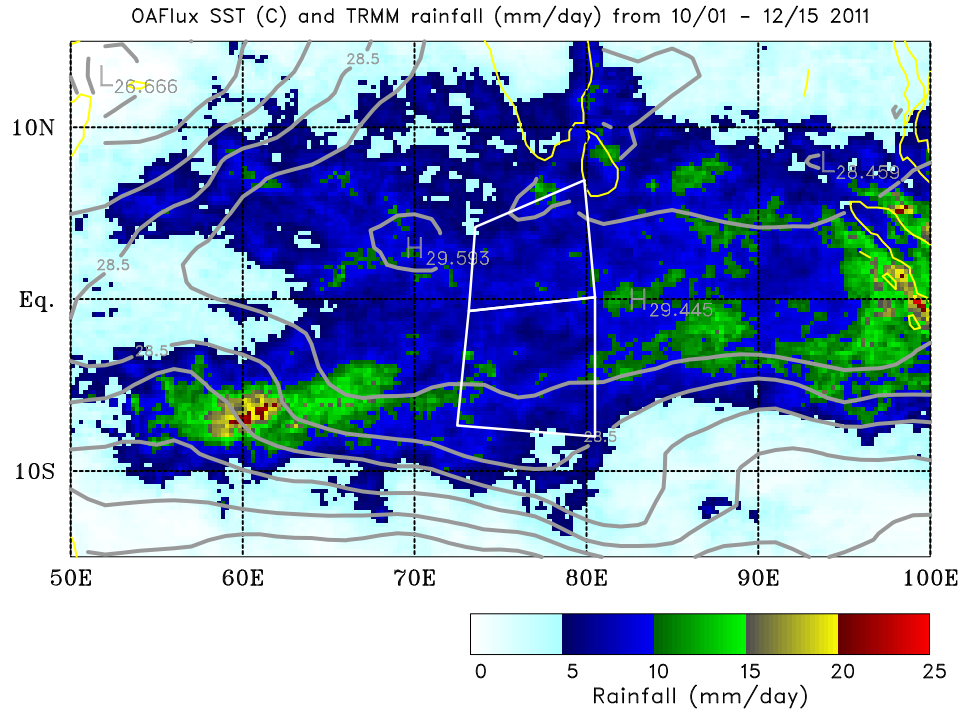


FIG. 4. TRMM 3B42 precipitation (mm day^{-1}) and OAFlux SST (C) for the DYNAMO period 1 October – 15 December 2011. Polygons indicate the two DYNAMO sounding arrays.

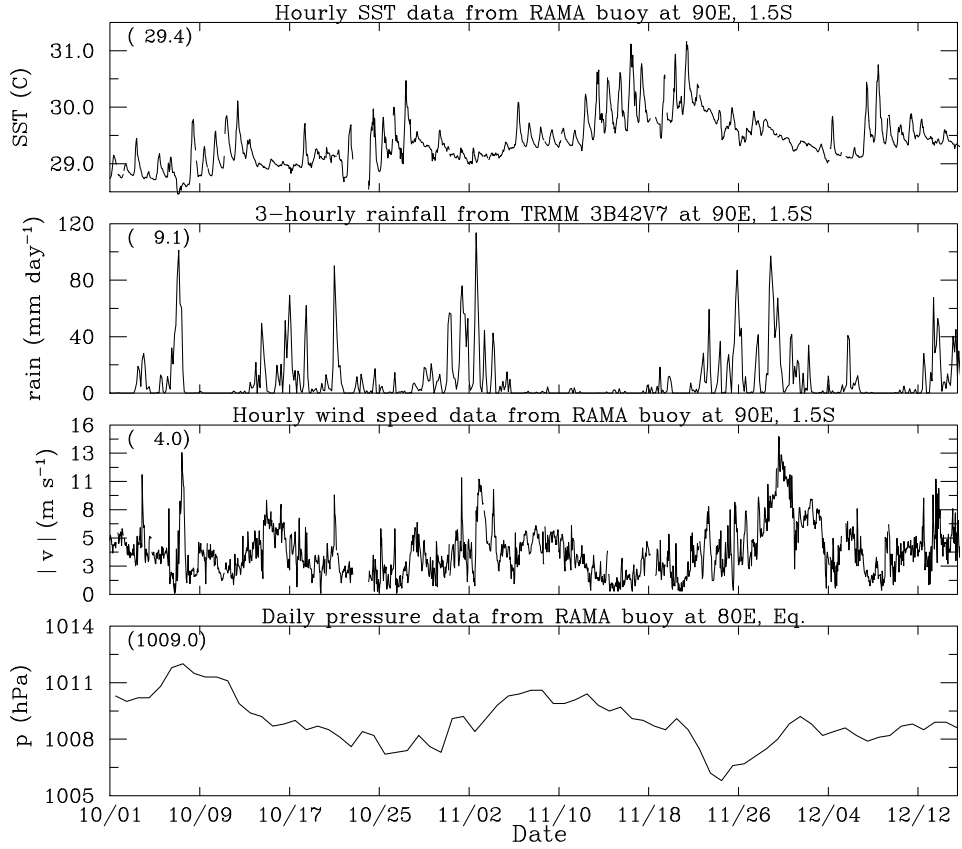
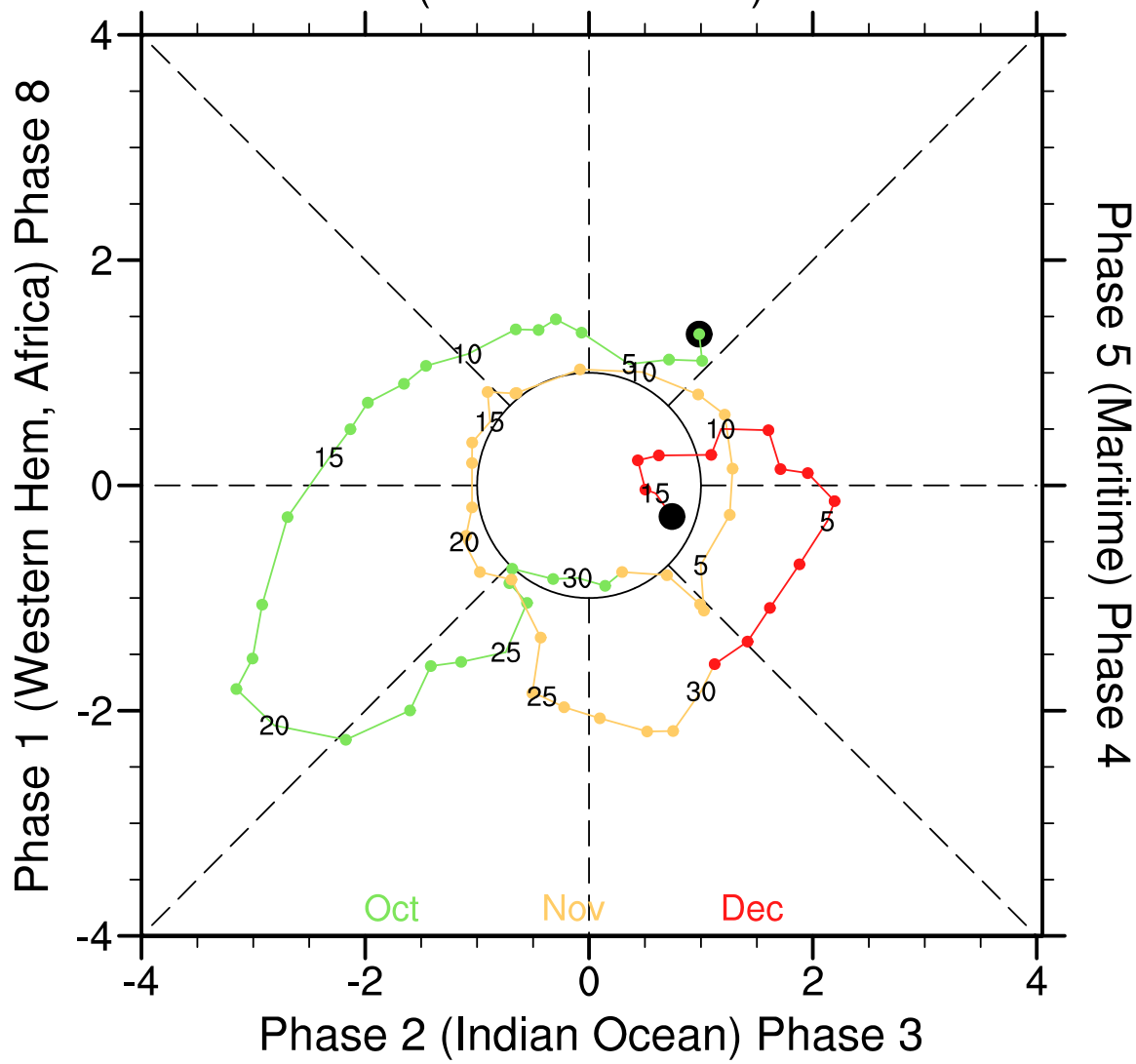


FIG. 5. Time series (from top to bottom) of hourly sea-surface temperature ($^{\circ}\text{C}$) at 1.5-m depth for DYNAMO SOP based on data from the RAMA buoy at 1.5°S 90°E , time series of 3-hourly average TRMM 3B42 rainfall (mm h^{-1}) within a 1° radius of same buoy, hourly wind speed (m s^{-1}) at same buoy, and time series of daily-averaged sea level pressure (hPa) at RAMA buoy at equator and 80.5°E .

MJO Phase: 15S-15N: 20111001-20111215

Phase 7 (Western Pacific) Phase 6



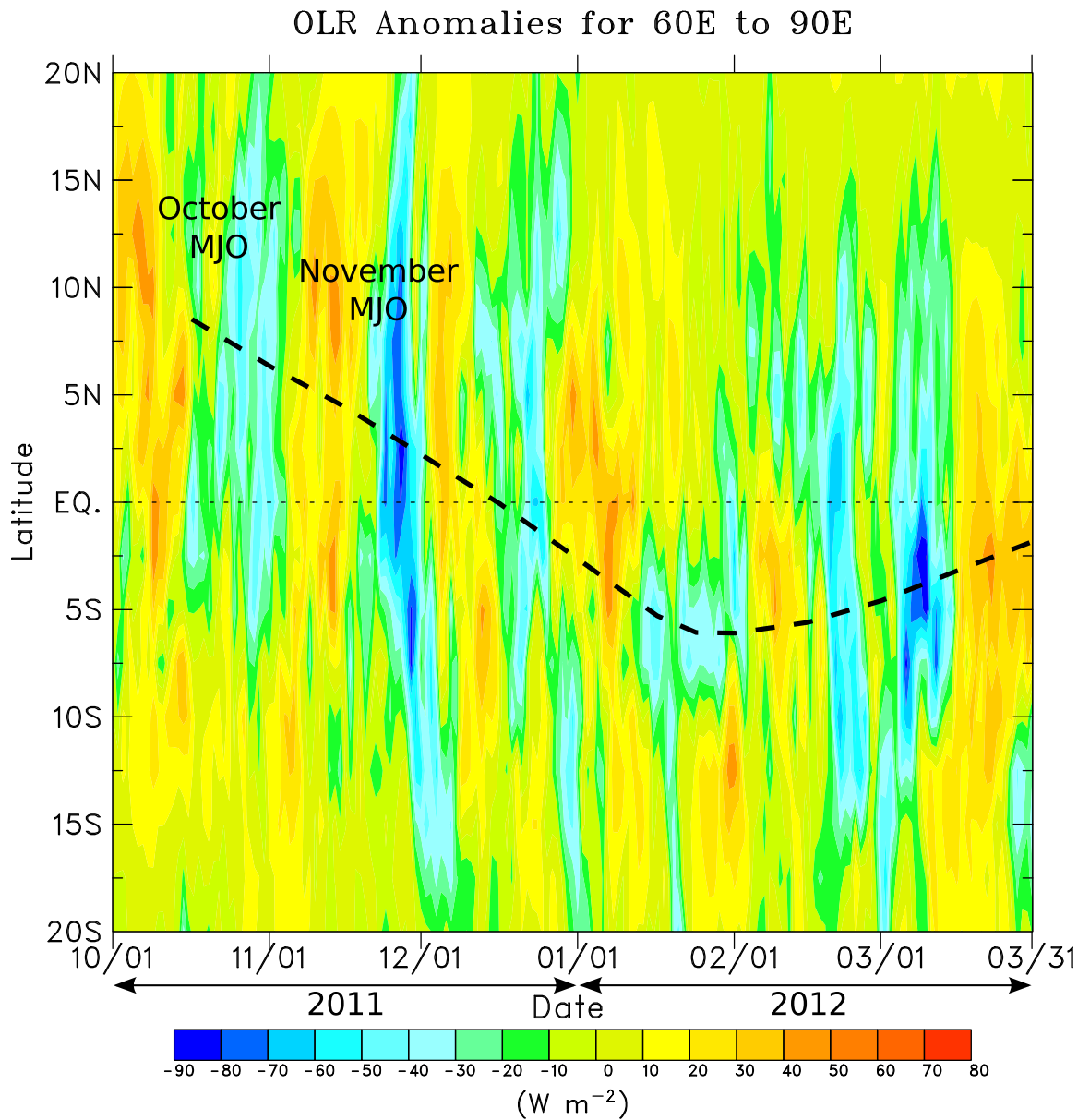


FIG. 7. Time-latitude plot of Outgoing Longwave Radiation (OLR) anomalies (W m^{-2}) computed from 1981-2010 long-term mean from 20°N to 20°S averaged from 60 to 90°E for period 1 October 2011-31 March 2012. Approximate seasonal track of anomaly centroid centers is indicated. October and November MJO active phases are denoted.

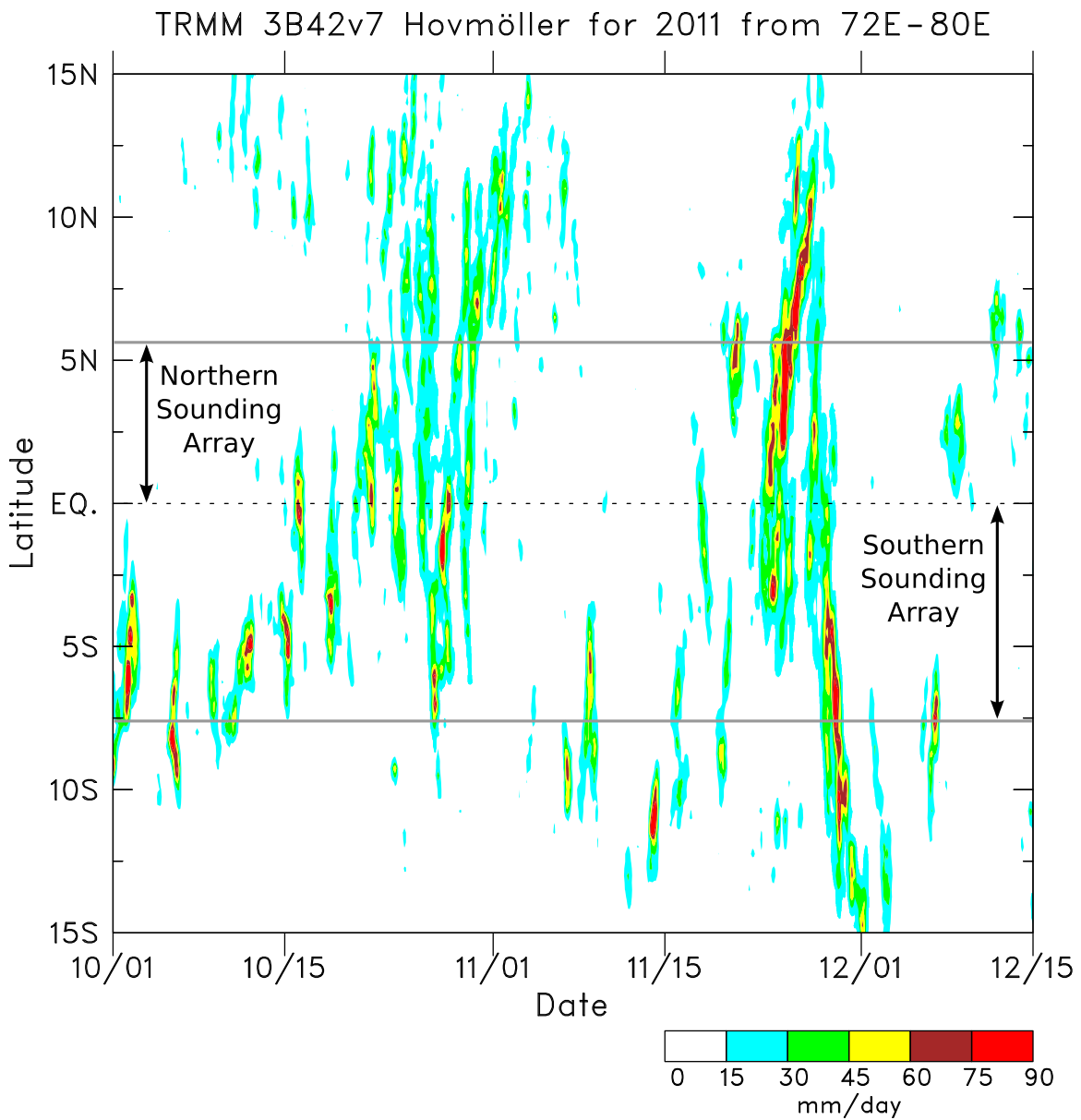


FIG. 8. Time-latitude plot of TRMM 3B42 precipitation (mm day^{-1}) from 15°N to 15°S averaged from 72 to 80°E for the period 1 October–15 December 2011. Latitudinal extents of northern and southern sounding arrays are indicated.

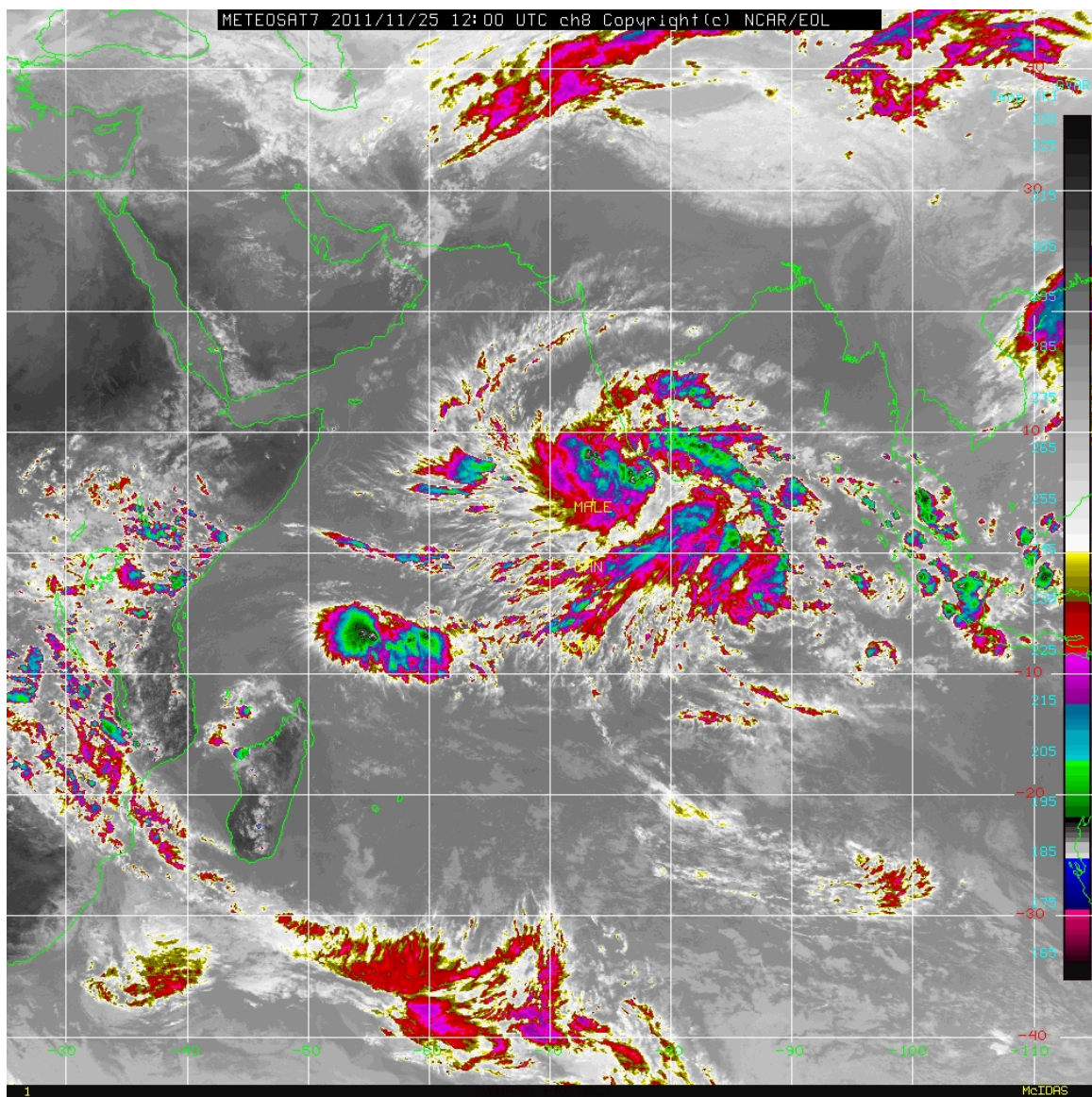


FIG. 9. Meteosat thermal IR image for 1200 UTC 25 November 2011. The tropical depression near the south tip of India became Tropical Storm 05A on 26 November.

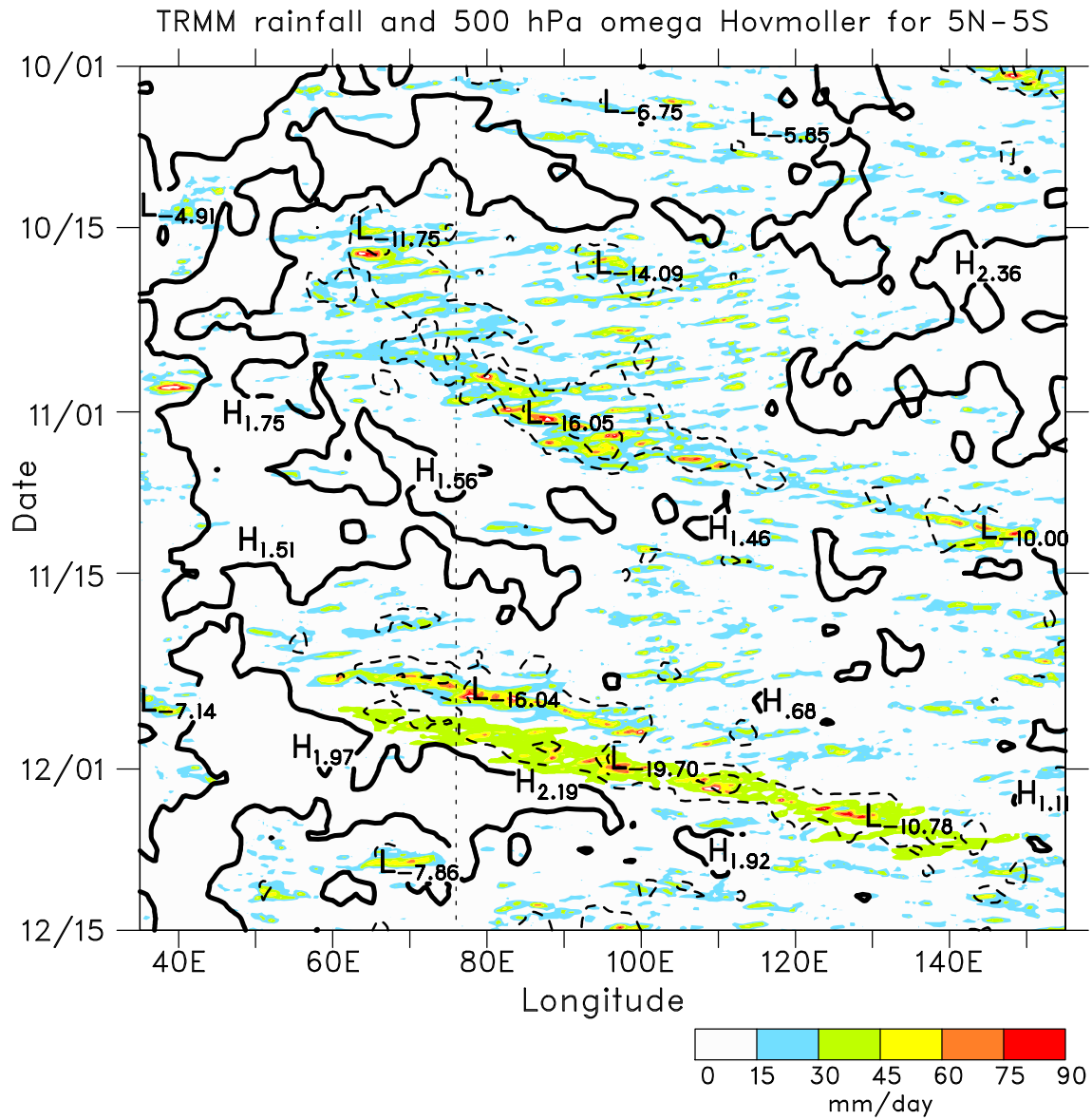


FIG. 10. Time-longitude plot of TRMM 3B42 precipitation (mm day^{-1}) and ECMWF 500-hPa vertical p -velocity (hPa h^{-1}) from 35° to 155°E averaged from 5°N to 5°S for the period 1 October–15 December 2011. Heavy solid line is zero contour; dashed contours indicate upward motion with contour interval of 10 hPa h^{-1} . Vertical dashed line denotes center of DYNAMO sounding arrays.

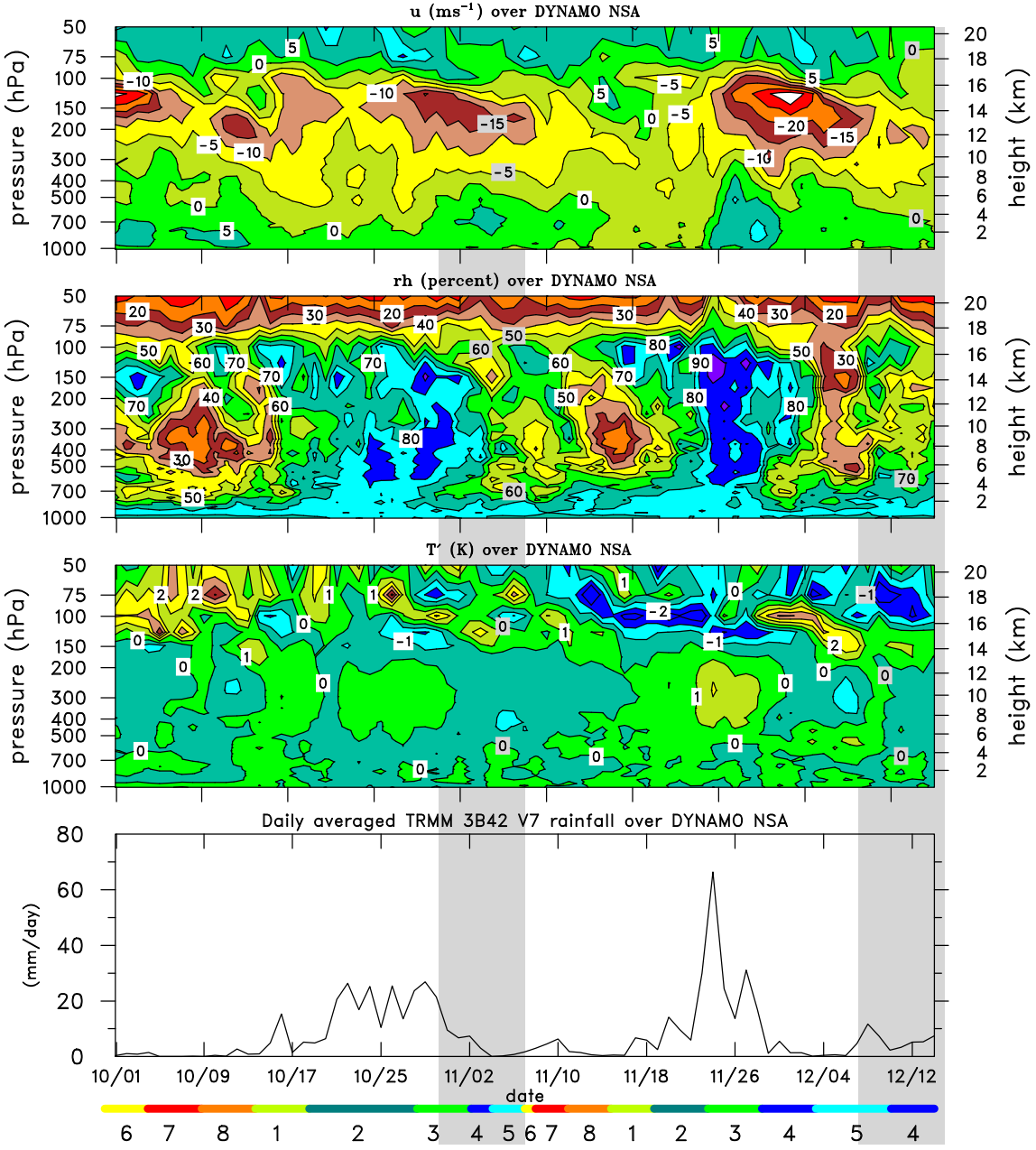


FIG. 11. Time series over northern sounding array (from top to bottom) of zonal wind (m s^{-1}), relative humidity (%; with respect to ice for $T < 0^{\circ}\text{C}$), temperature anomaly ($^{\circ}\text{C}$), and daily-averaged TRMM 3B42 rainfall (mm day^{-1}). Winds and thermodynamics are based on daily averages of six-hourly soundings, with temperature anomaly based on SOP mean. Color bars at bottom refer to phases of RMM index shown in Fig. 6. Vertical shaded bars indicate times when R/V *Revelle* was off station.

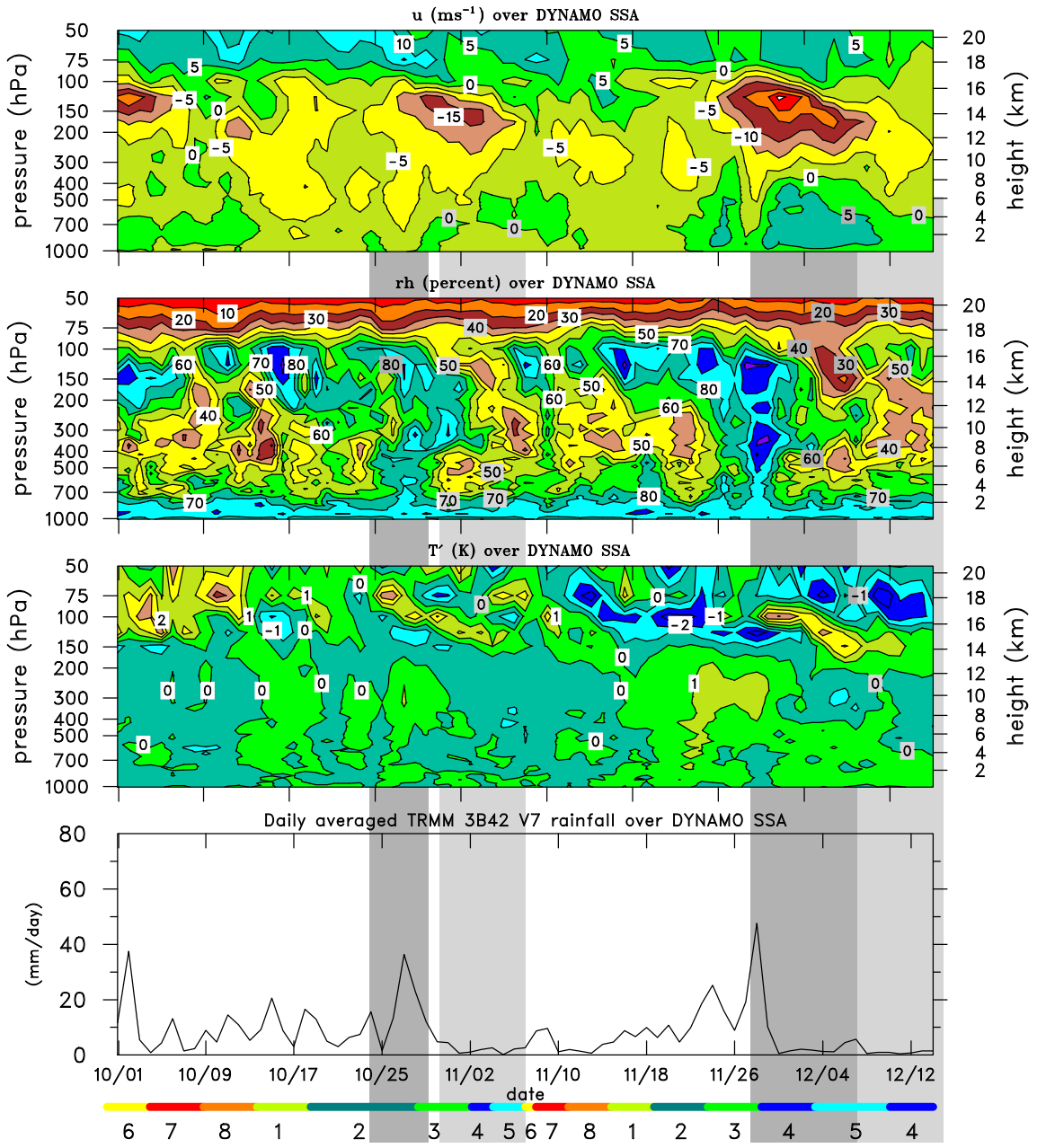


FIG. 12. As in Fig. 11, except for southern sounding array. Dark and light vertical shaded bars indicate times when R/V *Mirai* and *Revelle*, respectively, were off station.

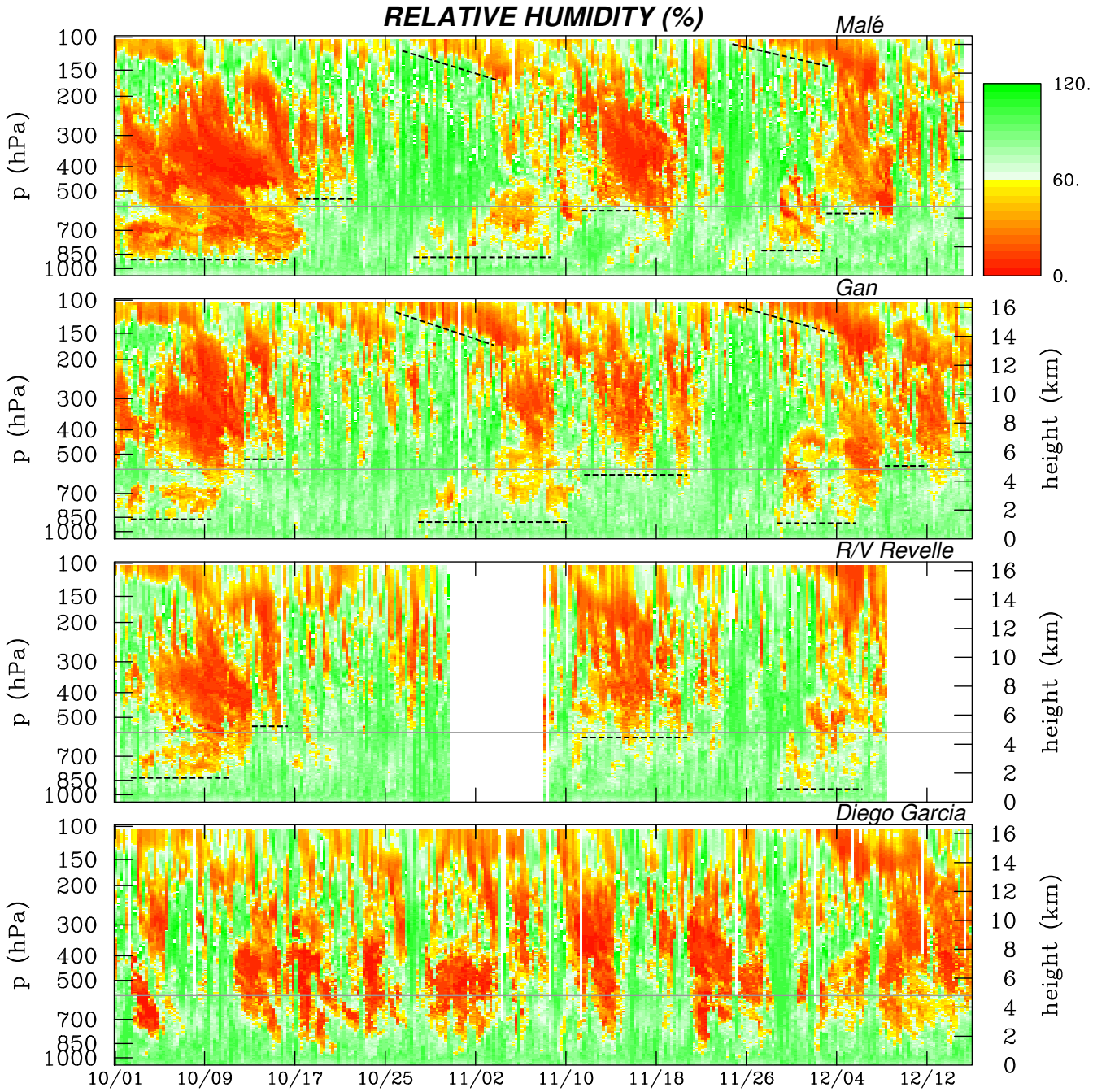


FIG. 13. Time series of relative humidity (%), with respect to ice for $T < 0^\circ\text{C}$) from 1 October to 15 December at Malé, Gan Island, R/V Revelle, and Diego Garcia based on full time resolution of sounding data. See Fig. 1 for site locations. Dotted line segments denote approximate tops of moist layers. Thin white line denotes 0°C level.

Basic fields for 01 Oct - 30 Nov 2011

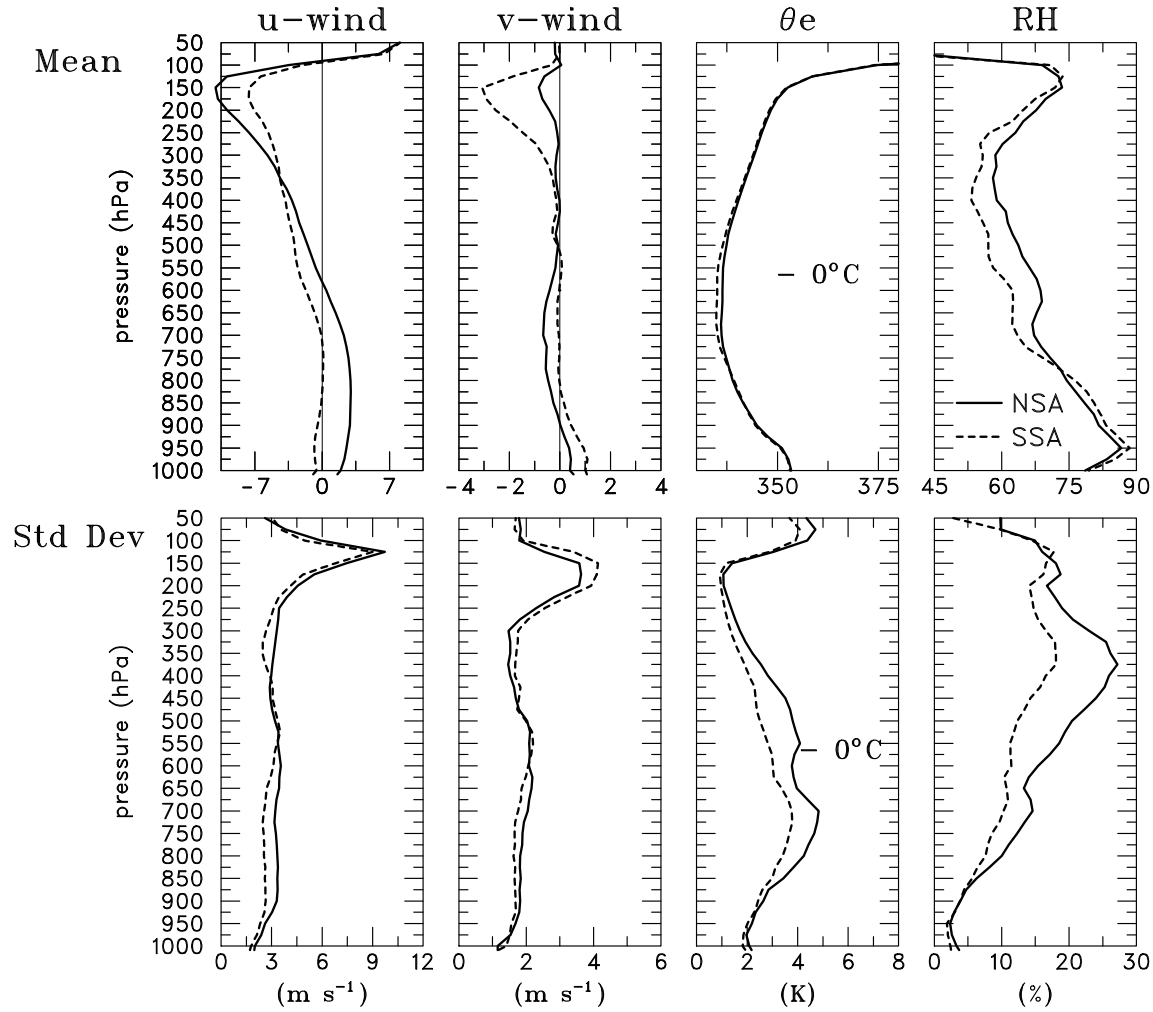


FIG. 14. (top) Two-month (1 October-30 November) mean vertical profiles of zonal and meridional wind (m s^{-1}), equivalent potential temperature (K), and relative humidity (with respect to ice for $T < 0^{\circ}\text{C}$), and (bottom) standard deviations of these variables for the northern (solid) and southern (dashed) sounding arrays.

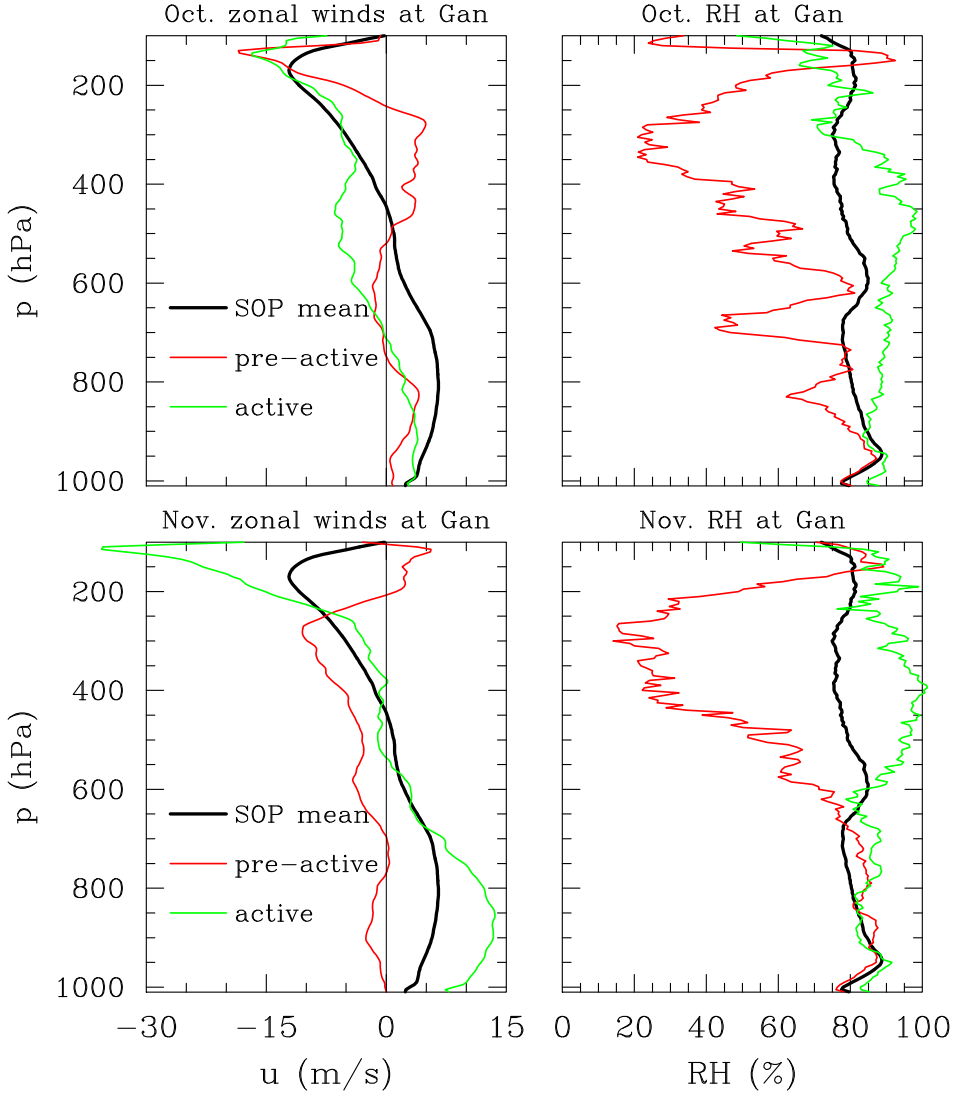


FIG. 15. Mean, pre-active, and active phase profiles of (left) zonal wind (m s^{-1}) and (right) relative humidity (%) with respect to ice for $T < 0^\circ\text{C}$ for (top) October and (bottom) November. Pre-active and active dates are 5 and 26 for October and 16 and 27 for November.

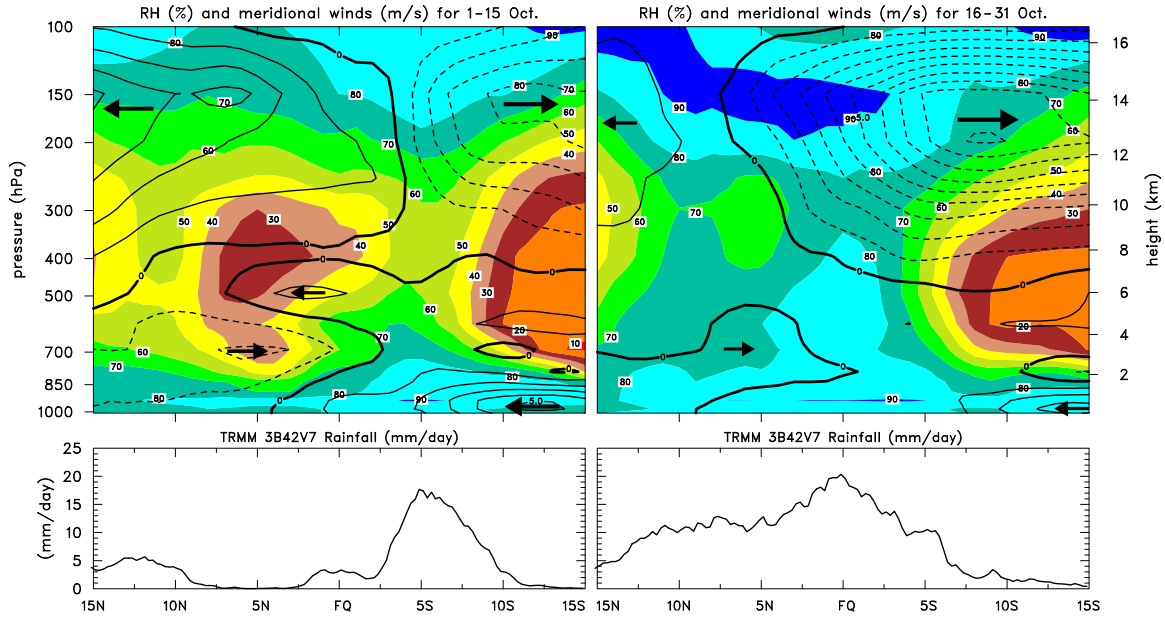


FIG. 16. North-south cross section through sounding arrays of ECMWF operational analysis (top) relative humidity (%), with respect to ice for $T < 0^\circ\text{C}$) and meridional wind (contour interval: 1 m s^{-1}), and (bottom) TRMM 3B42 rainfall for periods (left) 1-15 October and (right) 16-31 October 2011.

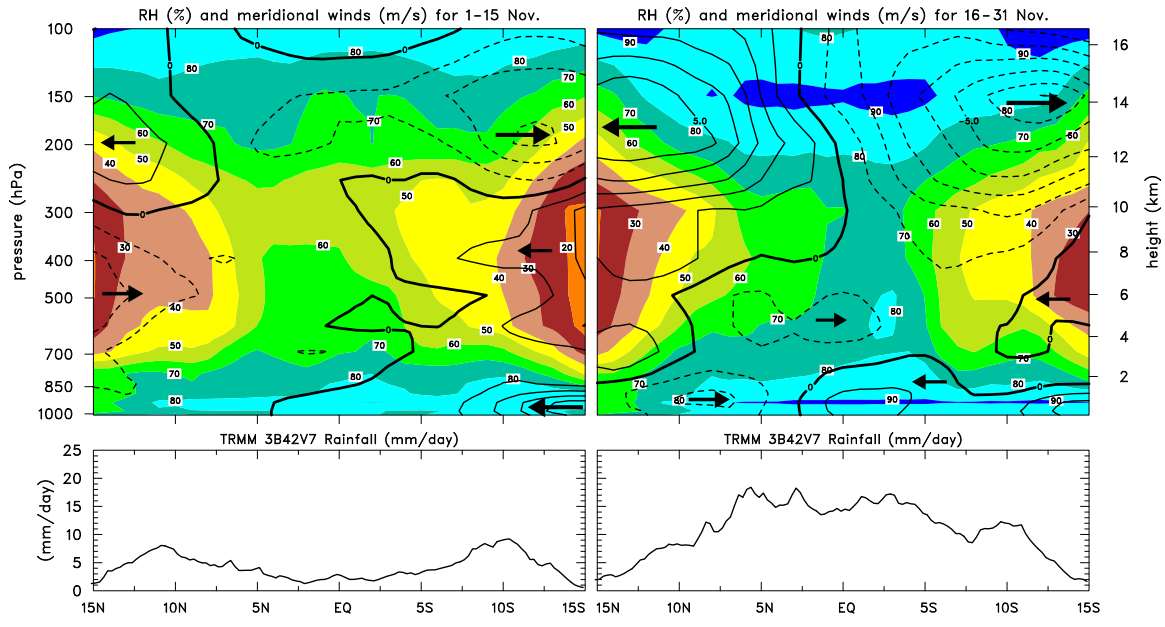


FIG. 17. As in Fig. 16, except for periods (left) 1-15 November and (right) 16-30 November 2011.

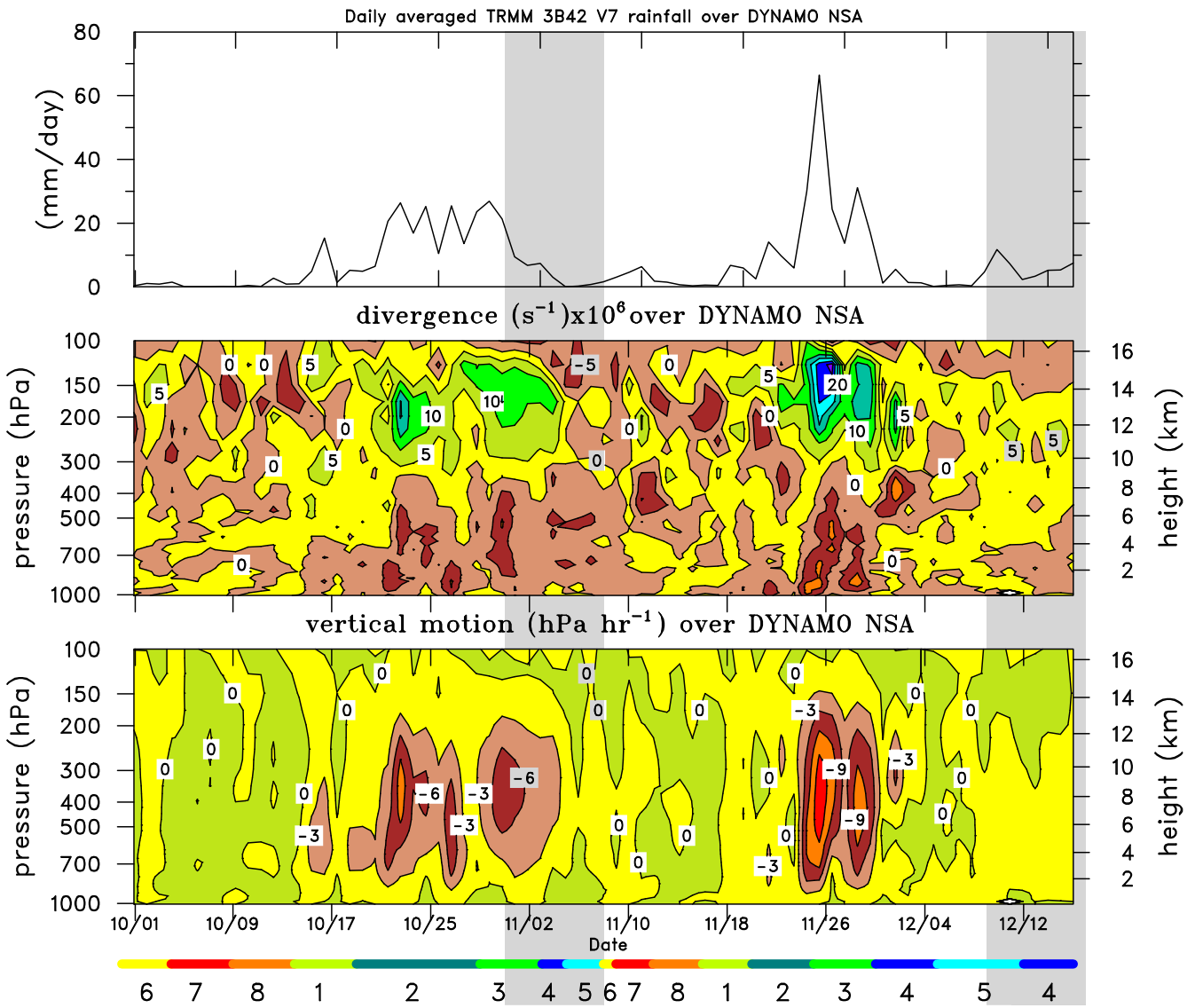


FIG. 18. SOP time series of (top) TRMM 3B42 rainfall, (middle) uncorrected divergence ($10^{-6} s^{-1}$), and (bottom) vertical motion ($hPa h^{-1}$) for northern sounding array. Color bars at bottom refer to phases of RMM index shown in Fig. 6. Vertical shaded bars indicate times when R/V *Revelle* was off station.

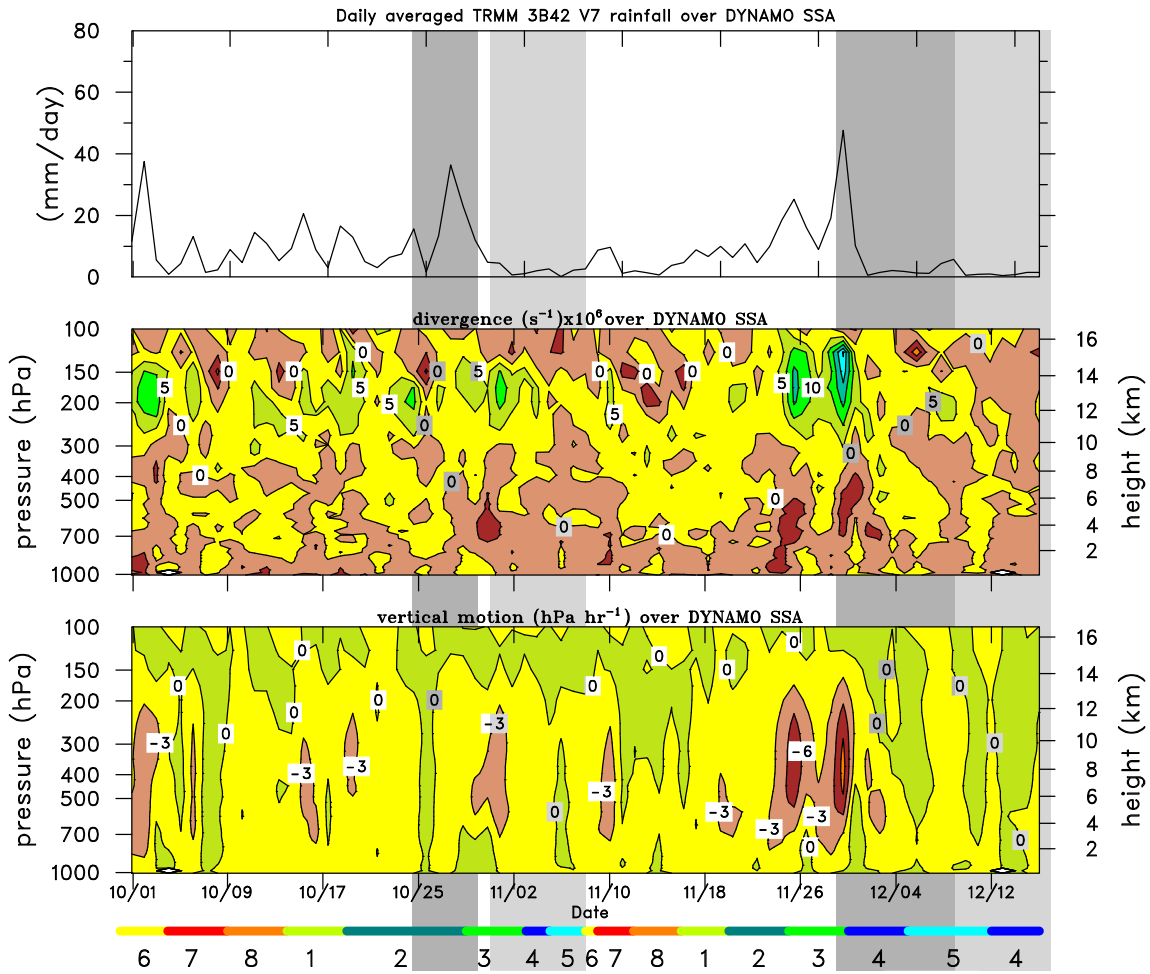


FIG. 19. As in Fig. 18, but for southern array. Dark and light vertical shaded bars indicate times when R/V *Mirai* and *Revelle*, respectively, were off station.

01 Oct.-30 Nov. diagnosed fields

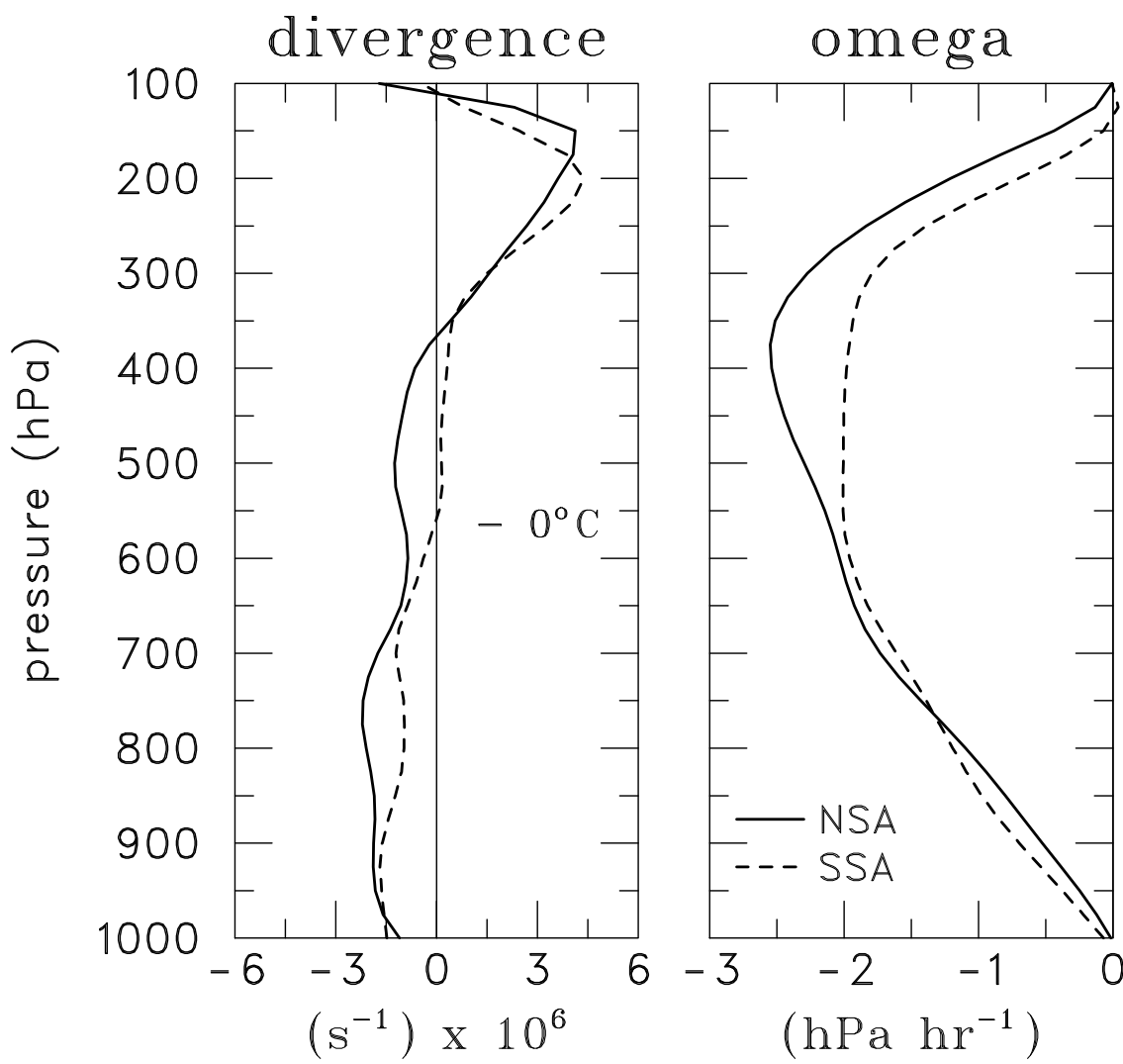


FIG. 20. 1 October-30 November mean vertical profiles of divergence (10^{-6} s^{-1}) and vertical motion (hPa hr^{-1}) for the northern (solid) and southern (dashed) sounding arrays.

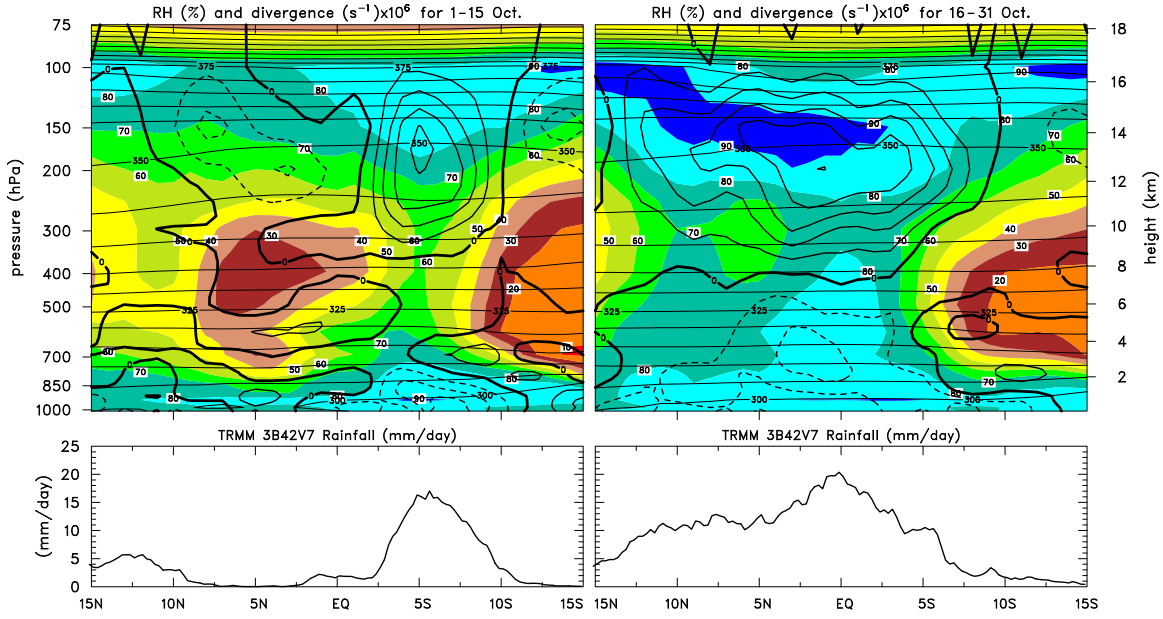


FIG. 21. North-south cross section through sounding arrays of ECMWF operational analysis (top) relative humidity (%), with respect to ice for $T < 0^\circ\text{C}$), horizontal divergence (contour interval: $2 \times 10^{-6} \text{ s}^{-1}$), and potential temperature (K, thin quasi-horizontal lines; contour interval: 5 K); and (bottom) TRMM 3B42 rainfall for periods (left) 1-15 October and (right) 16-31 October 2011.

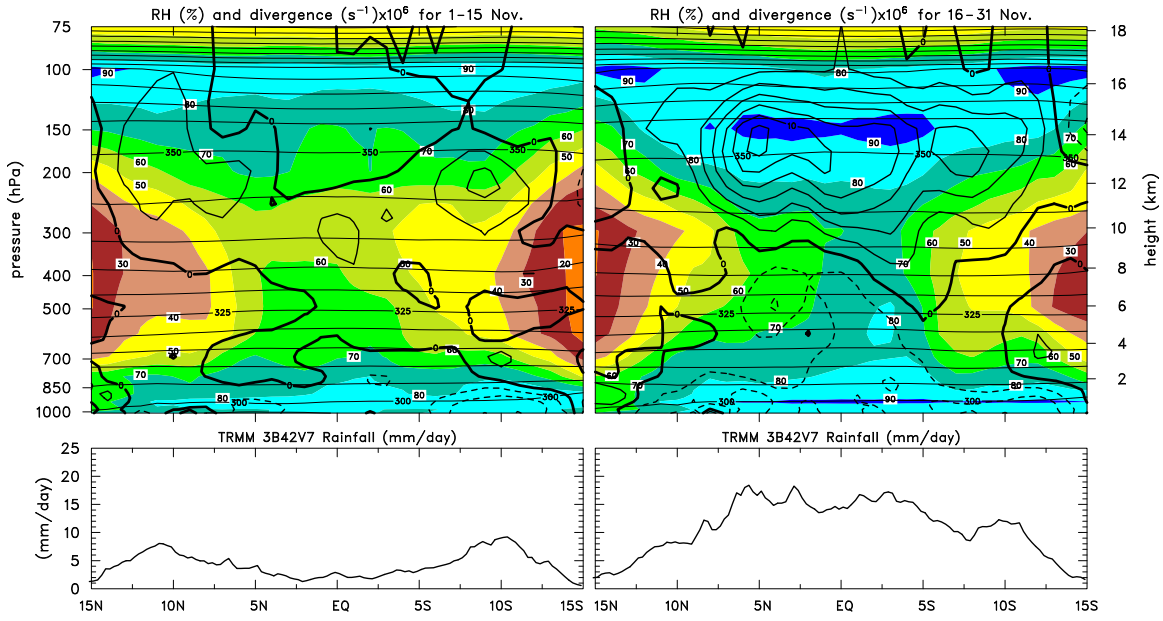


FIG. 22. As in Fig. 21, except for periods (left) 1-15 November and (right) 16-30 November 2011.

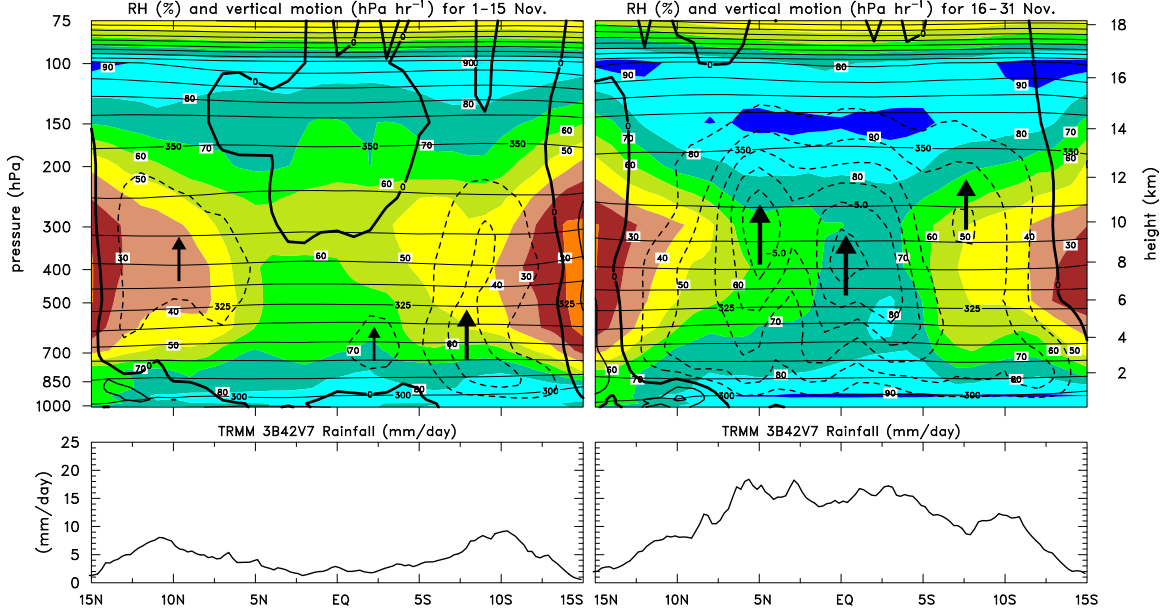


FIG. 23. North-south cross section through sounding arrays of ECMWF operational analysis (top) relative humidity (%), with respect to ice for $T < 0^\circ\text{C}$), vertical motion (contour interval: 1 hPa h^{-1}), and potential temperature (K, thin quasi-horizontal lines); and (bottom) TRMM 3B42 rainfall for periods (left) 1-15 November and (right) 16-30 November 2011.

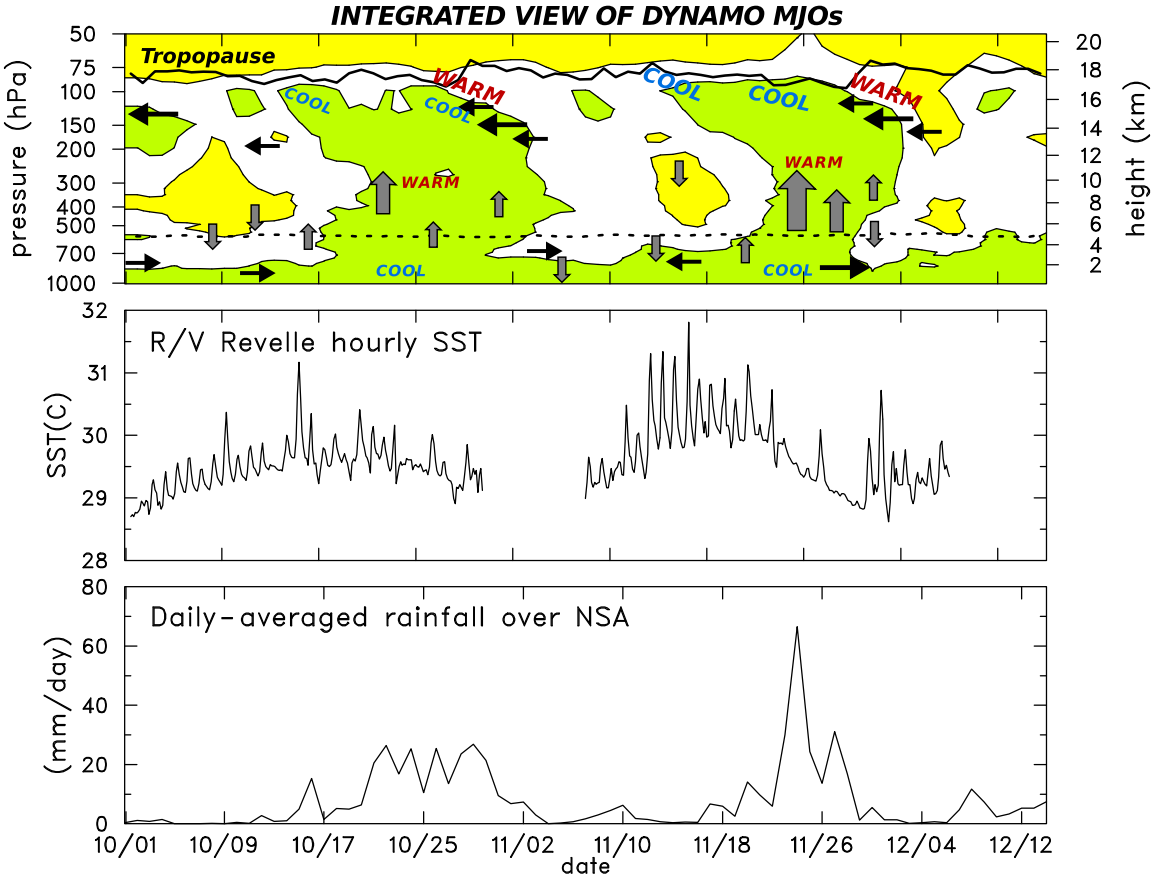


FIG. 24. (top panel) Integrated depiction of vertical structure of two MJOs during the period 1 October–15 December 2011 based on mean fields over northern sounding array. Green (yellow) shading denotes areas of relative humidity $> 70\%$ ($< 40\%$), respectively. Thin (broad) arrows denote locations of zonal wind (vertical motion) maxima. Centers of cool and warm temperature anomalies are shown. Relative magnitudes of features are represented by sizes of symbols. At upper levels, these anomalies have a tilted structure as do the easterly wind maxima. Daily-averaged 0°C level (dashed line) and cold-point tropopause level (solid line) are indicated. (middle panel) Hourly SST time series at R/V *Revelle*. (bottom panel) TRMM 3B42 daily-averaged rainfall rate over the northern sounding array.